

Phenomenological models of two-particle correlations on transverse momentum in relativistic heavy-ion collisions

R. L. Ray and A. Jentsch¹

¹*Department of Physics, The University of Texas at Austin, Austin, Texas 78712 USA*

(Dated: December 14, 2024)

Two-particle correlations on two-dimensional transverse momentum (p_{t1}, p_{t2}) constructed from the particle production in relativistic heavy-ion collisions allow unique access to soft, semi-hard and hard-scattering processes in these systems. Only a few measurements of this type are reported in the literature and phenomenological models, which facilitate physical interpretation of the correlation structures, are non-existent. On-going effort at the Relativistic Heavy-Ion Collider (RHIC) will provide a significant volume of these correlation measurements in the future. In this work two phenomenological models which describe 2D correlations on transverse momentum are developed and the results are compared to available data. One model is based on a collision event-by-event fluctuating blast wave. The other is based on an event-by-event fluctuating color-string plus jet fragmentation approach. Both models are shown to be capable of accurately describing the measured single-particle p_t distributions for minimum-bias Au+Au collisions at $\sqrt{s_{NN}} = 200$ GeV as a function of collision centrality. Both models are then applied to estimates of preliminary, charged-particle correlation measurements on 2D transverse momentum. The capabilities of the two models for describing the overall structure of these correlations and the stability of the fitting results with respect to centrality dependence are evaluated. Overall, both of these new, phenomenological approaches are capable of qualitatively describing the expected correlation structures on transverse momentum and will provide useful tools for interpreting the centrality trends in the forthcoming correlation data from the RHIC. Predictions of an event-by-event hydrodynamical model (EPOS) and a purely fragmentation-based model (HIJING) are compared to each other and to the preliminary correlation data.

PACS numbers: 25.75.-q, 25.75.Ag, 25.75.Gz

I. INTRODUCTION

Two-particle correlations constructed from the particles produced in high-energy, heavy-ion collision events convey information about partonic and hadronic dynamics throughout the spatio-temporal evolution of the hot, dense collision system. A number of processes are predicted to contribute to the correlations including both soft and hard quantum chromodynamics (QCD) scattering and fragmentation/hadronization [1–3], parton collective flow [4], gluon-gluon interference [5, 6], hadronization as affected by local conservation of momentum, charge and flavor, resonance decays, and final-state effects due to long-range Coulomb interactions and quantum interference [7]. The majority of reported correlation measurements are in terms of the number of particle pairs per angular bin which include projections onto azimuthal angle ϕ and/or pseudorapidity η ,¹ or onto relative azimuth $\phi_1 - \phi_2$ and/or relative pseudorapidity $\eta_1 - \eta_2$ [8]. The transverse momenta (p_t) of the two particles may also be restricted as in “trigger-associated” correlation studies [9]. The complementary pair-number correlations on transverse momentum (p_{t1}, p_{t2}), for a given (η, ϕ) acceptance or relative angular cuts, have received much less experimental and theoretical attention in the heavy-

ion physics literature. Such measurements have been reported by the NA49 Collaboration [10, 11], the CERES Collaboration [12], and the STAR Collaboration [13–15].

Two-particle correlations for symmetric, unpolarized collision systems (*e.g.* p+p, Au+Au, Pb+Pb but not p+Pb or polarized $\vec{p} + \vec{p}$ or $\vec{p} + \text{nucleus}$) near mid-rapidity are constant with respect to the summed variable $\phi_1 + \phi_2$ and approximately constant with respect to $\eta_1 + \eta_2$ [16, 17]. The correlations near mid-rapidity can therefore be described using four independent kinematic variables, for example $p_{t1}, p_{t2}, \eta_1 - \eta_2$, and $\phi_1 - \phi_2$ [15]. Correlation measurements on 2D $(\eta_1 - \eta_2, \phi_1 - \phi_2)$ angular space within 2D bins on transverse momentum space (p_{t1}, p_{t2}) should, in principle, represent all the statistically accessible information. Unfortunately, the absolute normalization of the 2D angular correlations is poorly determined due to multiplicity fluctuations arising from finite-width multiplicity bins [18, 19].² Measurements to date of 4D, two-particle correlations [20–23] are therefore incomplete.

In Ref. [24] it was shown that several measures of non-

¹ Pseudorapidity is defined as $\eta = -\ln[\tan(\theta/2)]$, where θ is the polar scattering angle relative to the beam direction.

² A derivation of normalized 2D angular correlations of binned total p_t , using an angular scale-dependent mean- p_t fluctuation method, is given in [18, 19]. Application of this method to normalize the pair-number angular correlations is problematic because the finite multiplicity bin-width contributes directly to event-wise multiplicity fluctuations in the angular bins.

statistical mean- p_t fluctuations from the literature can be used to define minimally biased two-particle pair-number correlations on (p_{t1}, p_{t2}) for arbitrary 2D angular acceptance or (η, ϕ) bin size (scale). These correlations determine the average value of the 2D angular correlations for each (p_{t1}, p_{t2}) bin, thus allowing the angular correlations to be normalized and enabling experimental measurements of 4D pair-number correlations to be completed.

Normalized correlation measurements on (p_{t1}, p_{t2}) provide experimental access to fluctuation processes which affect the particle p_t -distribution uniformly across the (η, ϕ) acceptance. For example, in hydrodynamic models with global equilibration and uniform transverse flow (but including elliptic flow relative to a reaction plane), the overall slope of the p_t distribution is determined by the kinetic freeze-out temperature and flow velocity. The last two quantities may vary from event-to-event due to initial-state fluctuations [25, 26]. The resulting angular correlations from a collection of such events contain no information about the initial-state other than the initial eccentricity [4]. Toy models presented by the NA49 and STAR Collaborations [11, 14] demonstrate that event-wise fluctuations in the overall slope of the p_t distribution produce a distinctive “saddle-shape” in the (p_{t1}, p_{t2}) correlation, similar to that observed in the data, thus allowing experimental access to this type of event-wise non-statistical (dynamical) fluctuation. The generic saddle-shape correlation, *i.e.* positive correlations along the $p_{t1} \approx p_{t2}$ main-diagonal at lower and higher p_t and negative correlations along the off-diagonal where $p_{t1} > p_{t2}$ or vice-versa, follows directly from the event-wise variation in the slope of the single-particle parent p_t distribution. The data represent one possible statistical sample of the parent distribution.

In addition, in heavy-ion collision models with jet fragmentation, *e.g.* HIJING [27], fluctuations in the p_t distribution and particle pair-number density occur in localized angular regions as the number and total energy of the jets fluctuate from event-to-event. These non-statistical fluctuations produce correlations in both relative-angle space and in (p_{t1}, p_{t2}) space. The former correlations yield the average number of jet related particle pairs per event, while the latter determines the variance of the fluctuating number of pairs, an independent quantity. Pair-number correlations on (p_{t1}, p_{t2}) in jet production models are sensitive to event-wise dynamical fluctuations in both the number and energy of the jets, thus providing access to additional dynamical information beyond that which can be studied with angular correlations alone.

The STAR Collaboration at the RHIC has reported preliminary measurements of pair-number correlations on (p_{t1}, p_{t2}) for Au+Au collisions at $\sqrt{s_{NN}} = 200$ GeV [20] which, when completed, will greatly increase the volume and quality of published transverse momentum correlation data. As indicated above, the literature related to pair-number correlations on transverse momentum is limited, and there is an absence of phenomenological models

to assist in the interpretation of the data. To address the latter, and in anticipation of the new STAR Collaboration results, the present work presents and tests the general efficacy and stability of two very different phenomenological models of (p_{t1}, p_{t2}) correlations for heavy-ion collisions at the RHIC and the Large Hadron Collider (LHC). The first is based on a fluctuating blast-wave (BW) model [28, 29]. The second is based on a fluctuating, two-component fragmentation (TCF) model motivated by the success of the Kharzeev and Nardi (KN) [30] “soft plus hard” two-component interaction model. In addition, we show predictions of the event-wise (3+1)-dimensional, viscous hydrodynamic model EPOS [25] by K. Werner *et al.* and the event-wise LUND [1] plus PYTHIA [2] combined fragmentation code HIJING by Wang and Gyulassy [27].

Phenomenological models play a more important role in the analysis of particle-pair number correlations on (p_{t1}, p_{t2}) than they do in the corresponding angular correlations. Correlation structures on angular coordinates, although not without ambiguities, can be more readily interpreted in terms of possible physical mechanisms [31, 32]. Examples include elliptic flow and the quadrupole correlation, dijets and the near-side 2D correlation peak plus an away-side (AS) non-quadrupole ridge, quantum correlations (HBT) and a sharp near-side peak, plus others [31, 32]. On the other hand, the correlation structures which have been observed so far on (p_{t1}, p_{t2}) are not so readily interpreted. Different dynamical mechanisms can produce similar structures, as will be shown in this paper. As a result, phenomenological models are necessary to help tease apart possible underlying mechanisms and to assist in the development of new theoretical models aimed at understanding these correlations.

This paper is organized as follows. The fluctuating BW and TCF models are derived in Secs. II and III, respectively, and are tested with respect to charged-particle p_t spectra data for Au+Au collisions at $\sqrt{s_{NN}} = 200$ GeV. In Sec. IV both models are further tested by comparing fitted results to approximate, analytical representations of preliminary $\sqrt{s_{NN}} = 200$ GeV Au+Au (p_{t1}, p_{t2}) correlation data from the STAR Collaboration [20, 21]. The general efficacy, centrality dependence, and parameter scalings of the models are also discussed in Sec. IV. EPOS and HIJING predictions for the 200 GeV Au+Au collision system are presented and discussed in Sec. V. A summary and conclusions are given in Sec. VI.

II. BLAST-WAVE MODEL WITH FLUCTUATIONS

A. Single-particle distribution

The fluctuating blast-wave model is based on the invariant phase-space source emission distribution of Schnedermann, Sollfrank and Heinz (SSH) [28] and as further developed by Tomášik, Wiedemann and

Heinz [29]. In this model the invariant momentum distribution is calculated by integrating over the space-time coordinates of the source function $S(x, p)$ where

$$\begin{aligned} E \frac{d^3 N}{dp^3} &= \frac{d^2 N}{2\pi m_t dm_t dy} = \int dx^4 S(x, p) \\ &= \int \tau d\tau \int d\eta_s \int r dr \int d\varphi S(x, p), \end{aligned} \quad (1)$$

x, p are four-vectors, E is the total energy of the particle, $m_t = \sqrt{p_t^2 + m_0^2}$ is the transverse mass, and m_0 is assumed to be the pion rest-mass. Space-time coordinates τ , η_s , r , and φ are the proper time, source rapidity defined by $(1/2) \ln[(t+z)/(t-z)]$, transverse radius, and azimuthal angle, respectively. From Ref. [29] Eq. (1) can be expressed at mid-rapidity ($y = 0$) as

$$\begin{aligned} E \frac{d^3 N}{dp^3} &= \frac{\tau_0 m_t}{4\pi^2 \hbar^3} \int_0^\infty r dr G(r) e^{\beta \mu_0} I_0[\beta p_t \sinh \eta_t(r)] \\ &\times \int_{-\infty}^\infty d\eta_s \cosh \eta_s H(\eta_s) \exp[-\beta m_t \cosh \eta_t(r) \cosh \eta_s] \end{aligned} \quad (2)$$

where τ_0 is the mean emission proper time, $\beta = 1/T$ is the inverse temperature, μ_0 is the chemical potential, I_0 is a modified Bessel function, $G(r)$ and $H(\eta_s)$ are the transverse and longitudinal-rapidity source distributions, and $\eta_t(r)$ is the transverse flow rapidity. The latter is defined in terms of the transverse flow velocity $v_t(r)$, where

$$\eta_t(r) = \frac{1}{2} \ln \left(\frac{1 + v_t(r)}{1 - v_t(r)} \right) \quad (3)$$

and the flow velocity profile is assumed to follow a power-law distribution given by [33]

$$v_t(r) = a_0 \varrho^{n_{\text{flow}}}, \quad \varrho \equiv r/R_0, \quad (4)$$

where R_0 is the transverse radius parameter of the source. The transverse flow velocity is equal to $\tanh \eta_t(r)$.

In deriving Eq. (2) we assumed Bjorken boost invariant expansion [29, 34] (longitudinal flow rapidity equals η_s), which is conventional in BW models. The source distribution was assumed to be uniform on azimuth, *e.g.* no $\cos(n\phi)$ dependence where $n \geq 2$, because the final-state particle yield is integrated over angular intervals of either π or 2π . We also assumed the following in order to simplify the model, to focus on the dominant sources of fluctuations in the p_t distribution, and to simplify the numerical integrations: (1) the Maxwell-Boltzmann limit for the emission function, (2) a constant chemical potential $\mu(r) \approx \mu_0$, (3) a constant source distribution $G(r)$ from $r = 0$ to maximum radius R_0 , and (4) the shape of source distribution $H(\eta_s)$ is taken from measured $dN_{\text{ch}}/d\eta$ distributions. Specifically, $H(\eta_s)$ is taken to be symmetric about $\eta_s = 0$ for symmetric collision systems and is represented by a modified Woods-Saxon distribution given by

$$H(\eta_s) = H(|\eta_s|) = \mathcal{N}_s \frac{1 + w|\eta_s|^2}{1 + \exp[(|\eta_s| - c)/z]}, \quad (5)$$

where \mathcal{N}_s is a normalization constant and parameters w , c and z were fitted to the $dN_{\text{ch}}/d\eta$ distributions for minimum-bias Au+Au collisions at $\sqrt{s_{\text{NN}}} = 200$ GeV reported by the PHOBOS Collaboration [35]. Parameter values $w = 0.02$, $c = 3.45$ and $z = 0.73$ approximately describe the shapes of these data at each measured centrality.

For applications to correlations on transverse momentum it is beneficial to display results on transverse rapidity, defined by $y_t = \ln[(p_t + m_t)/m_0]$ at mid-longitudinal rapidity, where $p_t = m_0 \sinh(y_t)$. Plotting the correlations on transverse rapidity rather than p_t enhances the visual access to correlation structures at both lower and higher p_t . In addition, transverse rapidity is an additively boost-invariant coordinate which facilitates studies of transverse fragmentation, *i.e.* jets. The single-particle distribution on y_t at $y = 0$ (longitudinal rapidity) is given by

$$\begin{aligned} \frac{d^2 N}{dy_t d\eta} &= 2\pi p_t \frac{dp_t}{dy_t} \frac{dy}{d\eta} \left(\frac{d^2 N}{2\pi m_t dm_t dy} \right) \\ &= 2\pi p_t^2 \left(\frac{d^2 N}{2\pi m_t dm_t dy} \right) \end{aligned} \quad (6)$$

where $m_t dm_t = p_t dp_t$, and $\eta = \lim_{m_0 \rightarrow 0} y$ is pseudorapidity. Jacobians dp_t/dy_t and $dy/d\eta$ equal m_t and p_t/m_t , respectively, at mid-rapidity. The quantity in parentheses in Eq. (6) is either taken from experiment or calculated in the blast-wave model.

A collection of collision events within a centrality bin can be expected to have fluctuating properties due to fluctuating initial-conditions [25, 26] and the stochastic nature of the system evolution from the initial impact to final kinetic decoupling. Within the context of the BW model we would therefore expect the source geometry, freeze-out temperature, and transverse flow to fluctuate from event-to-event. Furthermore, the temperature and flow fields within each collision environment might also vary relative to the smooth, analytic distribution assumed in Eq. (2). Fluctuations in τ_0 , G , H , μ_0 , β and η_t are therefore possible.

To account for these fluctuations we calculate the ensemble average of event-wise fluctuating BW distributions for non-identified, charged-particles. The distributions are binned on y_t with uniform bin width ϵ_{y_t} , and within mid-rapidity acceptance $\Delta\eta$ [*e.g.* $\Delta\eta = 2$ for the STAR Time Projection Chamber (TPC) tracking detector [36]]. The measured and BW model charged-particle distributions are related as follows,

$$\begin{aligned} \bar{\rho}_{\text{ch}}(y_t) &= \Delta\eta \epsilon_{y_t} \frac{d^2 N_{\text{ch,exp}}}{dy_t d\eta} \\ &= \Delta\eta \epsilon_{y_t} \frac{1}{\epsilon} \sum_{j=1}^{\epsilon} \frac{d^2 N_{\text{BW},j}}{dy_t d\eta} + \delta\bar{\rho}(y_t) \\ &\equiv \bar{\rho}_{\text{BW}}(y_t) + \delta\bar{\rho}(y_t), \end{aligned} \quad (7)$$

where the measured charged-particle distribution is introduced in the first line. In Eq. (7) the summation

includes ϵ collision events within a centrality event-class and $\delta\bar{\rho}(y_t)$ is the residual between the BW model and the spectrum data. Quantities $\bar{\rho}_{\text{ch}}(y_t)$ and $\bar{\rho}_{\text{BW}}(y_t)$ give the event-average number of charged-particles per y_t bin and are normalized to the measured number of charged particles produced within the acceptance, $y_t \in [y_{t,\text{min}}, y_{t,\text{max}}]$, $\Delta\eta$ and 2π in azimuth. Throughout this paper overlines denote event-averages or other mean values.

Event averaging over τ_0 and μ_0 do not affect the shape of the distribution $\bar{\rho}_{\text{BW}}(y_t)$, and calculations show that fluctuations in $G(r)$, or in radius R_0 , and in $H(\eta_s)$ produce minor effects relative to those generated by fluctuations in β and $\eta_t(r)$. We therefore fix τ_0 , μ_0 , $G(r)$ and $H(\eta_s)$ and only allow β and $\eta_t(r)$ to fluctuate from event-to-event as well as within the source distribution of each collision. Flow fluctuations are introduced by allowing the transverse flow rapidity to fluctuate about its nominal value where in the following calculations $\eta_t(r)$ in Eq. (3) is replaced with $\eta_{t0}\eta_t(r)$ where η_{t0} is a random variable sampled from a peaked distribution whose variance is an adjustable parameter.

The BW distribution in Eq. (7), including the above fluctuations, can be expressed as

$$\begin{aligned}\bar{\rho}_{\text{BW}}(y_t) &= \frac{1}{\epsilon} \sum_{j=1}^{\epsilon} \rho_{\text{BW},j}(y_t) \\ &= \frac{1}{\epsilon} \sum_{j=1}^{\epsilon} \sum_{\beta} \sum_{\eta_{t0}} \rho_{\text{BW},j\beta\eta_{t0}}(y_t)\end{aligned}\quad (8)$$

where $\rho_{\text{BW},j\beta\eta_{t0}}(y_t)$ is the number of charged-particles in event j in an arbitrary y_t bin which was emitted from the source region(s) having the discrete, binned values of inverse temperature (β) and transverse-flow rapidity scaling parameter (η_{t0}). The corresponding bin widths for variables β and η_{t0} are ϵ_{β} and $\epsilon_{\eta_{t0}}$.

To proceed further, Eq. (8) will be converted to an integral form by first reversing the summation order and then defining the following particle sums:

$$N_{\beta\eta_{t0}} \equiv \sum_{y_t} \sum_{j=1}^{\epsilon} \rho_{\text{BW},j\beta\eta_{t0}}(y_t), \quad (9)$$

$$N_{\beta} \equiv \sum_{\eta_{t0}} N_{\beta\eta_{t0}}, \quad (10)$$

$$N \equiv \sum_{\beta} N_{\beta}. \quad (11)$$

Sum $N_{\beta\eta_{t0}}$ is the total number of particles in ϵ events emitted from all regions having the same binned values of β and η_{t0} ; N_{β} is similarly defined; N is the total number of particles emitted into the acceptance from all ϵ events.

With these definitions Eq. (8) becomes

$$\begin{aligned}\bar{\rho}_{\text{BW}}(y_t) &= \sum_{\beta} \sum_{\eta_{t0}} \frac{1}{\epsilon} \sum_{j=1}^{\epsilon} \rho_{\text{BW},j\beta\eta_{t0}}(y_t) \\ &= \sum_{\beta} \sum_{\eta_{t0}} \frac{N}{\epsilon} \frac{N_{\beta}}{N} \frac{N_{\beta\eta_{t0}}}{N_{\beta}} \frac{1}{N_{\beta\eta_{t0}}} \sum_{j=1}^{\epsilon} \rho_{\text{BW},j\beta\eta_{t0}}(y_t) \\ &= \sum_{\beta} \sum_{\eta_{t0}} \bar{N} f_{\beta} g_{\beta,\eta_{t0}} \hat{\rho}_{\text{BW},\beta\eta_{t0}}(y_t) \\ &\approx \bar{N} \sum_{\beta} f_{\beta} \sum_{\eta_{t0}} g_{\eta_{t0}} \hat{\rho}_{\text{BW},\beta\eta_{t0}}(y_t) \\ &\rightarrow \bar{N} \int d\beta f(\beta, \bar{\beta}, q_{\beta}) \int d\eta_{t0} g(\eta_{t0}, \bar{\eta}_{t0}, \sigma_{\eta_t}) \hat{\rho}_{\text{BW},\beta\eta_{t0}}(y_t).\end{aligned}\quad (12)$$

In the preceding steps $\bar{N} = N/\epsilon$ is the mean multiplicity per collision, $f_{\beta} = N_{\beta}/N$ is the probability that a particle is emitted from a region with binned inverse temperature β , $g_{\beta,\eta_{t0}} = N_{\beta\eta_{t0}}/N_{\beta}$ is the probability that a particle within a β region is emitted from a sub-region having binned transverse flow parameter η_{t0} , and $\hat{\rho}_{\text{BW},\beta\eta_{t0}}(y_t)$ is the unit-normalized, event-average of the set of distributions $\rho_{\text{BW},j\beta\eta_{t0}}(y_t)$ in Eq. (8) where $\sum_{y_t} \hat{\rho}(y_t) = 1$. In the last two steps it was assumed, for computational simplicity and in the absence of credible models, that fluctuations in β and η_{t0} are independent (uncorrelated), where $g_{\beta,\eta_{t0}} \approx g_{\eta_{t0}}$. In the final line of Eq. (12) the continuum limit was assumed. Functions $f(\beta, \bar{\beta}, q_{\beta})$ and $g(\eta_{t0}, \bar{\eta}_{t0}, \sigma_{\eta_t})$ are emission probability densities which are assumed to be peaked functions determined by parameters $\bar{\beta}$, q_{β} and $\bar{\eta}_{t0}$, σ_{η_t} , respectively, which govern the means and variances of the two probability densities. Throughout this paper the “hat” symbol ($\hat{}$) denotes a unit-normalized distribution.

In applying the blast-wave model with fluctuating β and η_{t0} it was assumed that the regions where β and η_{t0} are greater than, or smaller than the mean, are randomly distributed throughout the source. With this assumption the summations in Eq. (12), for arbitrary values of β and η_{t0} , uniformly sample the entire source volume such that the resulting invariant momentum distribution is given by Eq. (2) when calculated with those specific β and η_{t0} values. Calculations of the emitted particle p_t spectrum from sources with either correlated β and η_{t0} fluctuations, or with position correlated β, η_{t0} fluctuations require microscopic models or Monte Carlo simulations, *e.g.* EPOS [25] and NEXSPHERIO [37], both of which are well beyond the scope and intent of the present phenomenological study.

In Ref. [14] it was shown that the transverse momentum spectrum data from relativistic heavy-ion collisions can be accurately described for $p_t < 5$ GeV/ c when the inverse temperature β of a Maxwell-Boltzmann distribution $\exp[-\beta(m_t - m_0)]$ samples a gamma distribution.

The unit-normal gamma distribution is given by

$$f_\gamma(\beta, \bar{\beta}, q_\beta) = \frac{q_\beta}{\bar{\beta}\Gamma(q_\beta)} \left(\frac{\beta q_\beta}{\bar{\beta}}\right)^{q_\beta-1} e^{-\beta q_\beta/\bar{\beta}} \quad (13)$$

where $\bar{\beta}$ is the mean and $1/q_\beta$ is the relative variance $\sigma_\beta^2/\bar{\beta}^2$. The above convolution integral gives [14]

$$\int_0^\infty d\beta f_\gamma(\beta, \bar{\beta}, q_\beta) e^{-\beta(m_t - m_0)} = [1 + \bar{\beta}(m_t - m_0)/q_\beta]^{-q_\beta}, \quad (14)$$

a Levy distribution [38].

The transverse flow rapidity scale parameter distribution was assumed to follow a similar peaked shape except with a suppressed long-range tail which helps the numerical integrations converge. The distribution was chosen to be a modified Gaussian given by

$$g(\eta_{t0}, \bar{\eta}_{t0}, \sigma_{\eta_t}) = \mathcal{N}_g \eta_{t0} \exp \left[-\frac{1}{2} \left(\frac{\eta_{t0} - \bar{\eta}_{t0}}{\sigma_{\eta_t}} \right)^2 \right] \quad (15)$$

where $\bar{\eta}_{t0} = 1$ (fixed) and \mathcal{N}_g normalizes the distribution to unity over the domain $\eta_{t0} \in [0, \infty]$.

The final form of the fluctuating blast-wave single-particle distribution is given by

$$\bar{\rho}_{\text{BW}}(y_t) = \bar{N} \int_0^\infty d\beta f_\gamma(\beta, \bar{\beta}, q_\beta) \int_0^\infty d\eta_{t0} g(\eta_{t0}, \bar{\eta}_{t0}, \sigma_{\eta_t}) \hat{\rho}_{\text{BW}, \beta \eta_{t0}}(y_t) \quad (16)$$

where

$$\hat{\rho}_{\text{BW}, \beta \eta_{t0}}(y_t) = \mathcal{N} m_t p_t^2 \frac{\tau_0 R_0^2 G_0 \Delta \eta \epsilon_{y_t}}{2\pi \hbar^3} \int_0^1 d\rho d\varrho e^{\beta \mu_0} I_0[\beta p_t \sinh \eta_t(\varrho)] \int_{-\infty}^\infty d\eta_s \cosh \eta_s H(\eta_s) e^{-\beta m_t \cosh \eta_t(\varrho) \cosh \eta_s} \quad (17)$$

Constant \mathcal{N} ensures that $\hat{\rho}_{\text{BW}, \beta \eta_{t0}}(y_t)$ is normalized to unity in the domain $y_t \in [y_{t\min}, y_{t\max}]$. The y_t -binned result in Eq. (17) was calculated at the mid-points of the y_t bins. In Eq. (17) the η_s integration was done numerically for discrete values of $\beta m_t \cosh \eta_t(\varrho)$ and saved for later interpolation during the 3D numerical integration over variables β , η_{t0} and ϱ . Integration limits and step sizes were studied to ensure sufficiently accurate convergence in the calculated y_t spectrum relative to the statistical errors in the data. The adjustable fit parameters in the single-particle BW model are $\bar{\beta}$ and q_β in Eq. (13), a_0 and n_{flow} in Eq. (4), and σ_{η_t} in Eq. (15) where \bar{N} is taken from data.

The blast-wave model was applied to the charged particle p_t spectra data for Au + Au minimum-bias collisions at $\sqrt{s_{\text{NN}}} = 200$ GeV measured by the STAR Collaboration [39] for collision centralities 0-5%, 5-10%, 10-20%, 20-30%, 30-40%, 40-60% and 60-80%. These data were fitted within the y_t range from 1.34 to 4.36, corresponding to p_t from 0.25 to 5.5 GeV/c. Three sets of fits were done in which (1) the full BW model was used where all five parameters above were freely varied, (2) a non-flowing ($a_0 = 0$), thermal fluctuation model was used, and (3) a non-fluctuating, pure BW model was used where $q_\beta = \sigma_{\eta_t} = 0$ while $\bar{\beta}$, a_0 and n_{flow} were freely varied. Best fits were based on minimum chi-square.

Quantitative descriptions of the data were obtained for all centralities using the full blast wave. Examples are shown in Fig. 1 for the 60-80%, 20-30% and 0-5% centralities where fits produced by the full BW, the non-flowing thermal fluctuation BW, and the non-fluctuating BW are shown by the solid, dashed and dotted curves, respectively. The BW model fit parameter values for all centralities and for each of the three model scenarios are listed in Table I. The residuals, $\delta \bar{\rho}(y_t)$ in Eq. (7), for the full BW model fits are of order 5% or less throughout the y_t and centrality ranges studied here.

The full BW model accurately describes the data over

the entire y_t range considered in this analysis. The non-flowing, thermal fluctuation BW model overestimates the mode (peak position) but accurately describes the data at larger y_t . The non-fluctuating BW model overestimates the peak position by an even larger amount and underestimates the data at low y_t less than 1.5 and at the largest y_t bin considered here.

Typical, non-fluctuating blast-wave model fits to p_t spectrum data produce results where the temperature decreases and the average flow velocity increases with centrality [40]. In the present BW model application, the average flow velocity increases slightly with centrality while the fitted temperature also increases. It should be noted that in the present application the fitting is performed over a larger p_t range than is usually addressed with blast-wave models [40] and the additional effects of fluctuations are included.

B. Two-particle distributions

Two-particle distributions were calculated by summing over all pairs of particles from the same collision (same-event pairs denoted “se”) for all events within a given centrality range. In the BW model, arbitrary pairs are

TABLE I: Blast-wave fit model parameters for the 200 GeV Au+Au minimum-bias p_t spectrum data from STAR [39] for the full BW model, the non-flowing BW, and the non-fluctuating BW as explained in the text. Data were fitted in the y_t range from 1.34 to 4.36 using 30 data points at each centrality. Temperature (T in GeV) equals $1/\beta$. Average transverse flow velocity \bar{v}_t equals $2a_0/(n_{\text{flow}} + 2)$ where $c = 1$ is assumed.

Centrality (%)	Full BW							No Flow BW			No Fluct. BW				
	T (GeV)	q_β	a_0	n_{flow}	σ_{η_t}	\bar{v}_t	χ^2_{DoF}	T (GeV)	q_β	χ^2_{DoF}	T (GeV)	a_0	n_{flow}	\bar{v}_t	χ^2_{DoF}
0-5	0.110	20.2	0.68	0.49	0.051	0.55	2.10	0.172	16.1	2.38	0.184	0.76	5.8	0.20	6.54
5-10	0.112	19.8	0.66	0.47	0.065	0.53	1.92	0.169	15.6	2.23	0.180	0.76	5.0	0.22	5.45
10-20	0.110	18.7	0.68	0.57	0.033	0.53	1.34	0.166	14.8	2.04	0.180	0.77	5.2	0.21	4.00
20-30	0.105	17.5	0.70	0.60	0.018	0.54	1.01	0.162	14.1	1.66	0.186	0.78	7.0	0.17	4.12
30-40	0.103	16.7	0.70	0.64	0.043	0.53	1.26	0.157	13.5	1.85	0.172	0.80	5.5	0.21	4.72
40-60	0.100	15.3	0.47	0.04	0.38	0.46	0.64	0.144	12.2	1.15	0.172	0.82	7.5	0.17	3.00
60-80	0.082	12.9	0.75	0.89	0.02	0.52	0.56	0.129	11.1	1.08	0.162	0.84	8.2	0.16	3.13

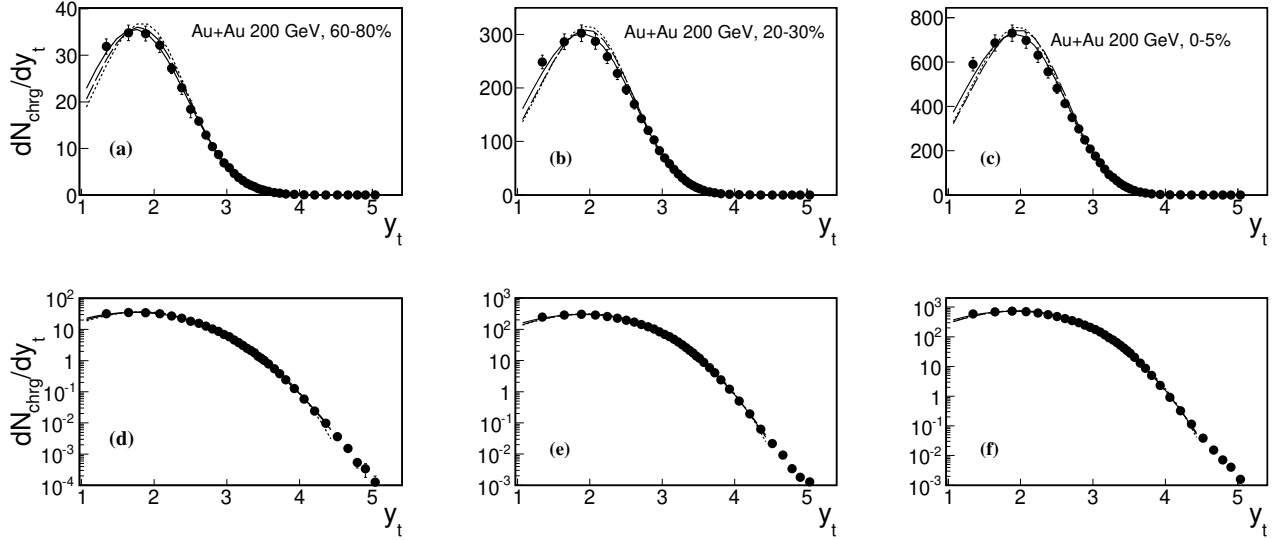


FIG. 1: Fluctuating blast-wave model fits to the 200 GeV Au+Au minimum-bias p_t spectrum data from STAR [39] showing only the 60-80%, 20-30% and 0-5% centrality results. Yields are shown as quantity dN_{ch}/dy_t versus transverse rapidity y_t as defined in the text, assuming pseudorapidity acceptance $\Delta\eta = 2$. Linear (upper row) and semi-log (lower row) plots are shown for the same data and curves to allow visual access to both lower and higher y_t fit results. Fit results assuming the full, non-flowing, and non-fluctuating BW models are shown by the solid, dashed and dotted curves, respectively, as explained in the text.

emitted from two, arbitrary regions of the source which are characterized by inverse temperature and transverse flow rapidity parameters (β_1, η_{t0_1}) and (β_2, η_{t0_2}) , respectively. Correlations arise when the distributions of (β_1, η_{t0_1}) versus (β_2, η_{t0_2}) are correlated [14]. As in the previous subsection, correlated fluctuations between β and η_{t0} are not considered; only (β_1, β_2) and $(\eta_{t0_1}, \eta_{t0_2})$ correlated fluctuations are included in the present model, both for computational simplicity and in lieu of credible models of 4D $(\beta_1, \eta_{t0_1}, \beta_2, \eta_{t0_2})$ correlated fluctuations.

In Ref. [24] it was shown that two-particle correlations on (y_{t1}, y_{t2}) are susceptible to statistical bias when collision events with varying multiplicities are combined. Several methods were proposed in that reference to eliminate the bias. Here, we use the correlation form derived from the mean- p_t fluctuation quantity $\Delta\sigma_{p_t:n}^2$ [41], where the

two-particle, same-event BW distribution is given by³

$$\bar{\rho}_{\text{BW,se}}(y_{t1}, y_{t2}) = \frac{1}{\epsilon} \sum_{j=1}^{\epsilon} \frac{\bar{N}}{n_j} \frac{n_j - 1}{n_j} [\rho_{\text{BW},j}(y_{t1}) + \delta\bar{\rho}(y_{t1})] \times [\rho_{\text{BW},j}(y_{t2}) + \delta\bar{\rho}(y_{t2})], \quad (18)$$

where n_j is the multiplicity in the acceptance of event j . For the present model application we may assume narrow multiplicity bin widths such that all events have fixed

³ Throughout this paper symbol ρ represents both single- and two-particle binned distributions. The number of y_t arguments distinguishes the usage.

multiplicity $n_j = \bar{N}$, in which case Eq. (18) simplifies to

$$\begin{aligned} \bar{\rho}_{\text{BW,se}}(y_{t1}, y_{t2}) = & \frac{\bar{N} - 1}{\bar{N}} \frac{1}{\epsilon} \sum_{j=1}^{\epsilon} [\rho_{\text{BW},j}(y_{t1}) \rho_{\text{BW},j}(y_{t2}) + \rho_{\text{BW},j}(y_{t1}) \delta \bar{\rho}(y_{t2}) \\ & + \rho_{\text{BW},j}(y_{t2}) \delta \bar{\rho}(y_{t1}) + \delta \bar{\rho}(y_{t1}) \delta \bar{\rho}(y_{t2})], \end{aligned} \quad (19)$$

where factor $(\bar{N} - 1)/\bar{N}$ normalizes the pair distribution to $\bar{N}(\bar{N} - 1)$, the number of pairs of particles per event counting both permutations.

The first term can be expanded similarly to the steps given in Eqs. (8)-(12). Defining this first term as $\bar{\rho}'_{\text{BW,se}}$ and introducing sums over fluctuating β and η_{t0} gives

$$\begin{aligned} \bar{\rho}'_{\text{BW,se}}(y_{t1}, y_{t2}) & \equiv (\bar{N} - 1)/\bar{N} \\ & \times \sum_{\beta_1, \eta_{t0_1}} \sum_{\beta_2, \eta_{t0_2}} \frac{1}{\epsilon} \sum_{j=1}^{\epsilon} \rho_{\text{BW},j\beta_1\eta_{t0_1}}(y_{t1}) \rho_{\text{BW},j\beta_2\eta_{t0_2}}(y_{t2}). \end{aligned} \quad (20)$$

Next, we define the following pair sums:

$$N_{\beta_1\eta_{t0_1}\beta_2\eta_{t0_2}} \equiv \sum_{y_{t1}, y_{t2}} \sum_{j=1}^{\epsilon} \rho_{\text{BW},j\beta_1\eta_{t0_1}}(y_{t1}) \rho_{\text{BW},j\beta_2\eta_{t0_2}}(y_{t2}), \quad (21)$$

$$N_{\beta_1\beta_2} \equiv \sum_{\eta_{t0_1}, \eta_{t0_2}} N_{\beta_1\eta_{t0_1}\beta_2\eta_{t0_2}}, \quad (22)$$

$$N_{(2)} \equiv \sum_{\beta_1, \beta_2} N_{\beta_1\beta_2} = \epsilon \bar{N}^2, \quad (23)$$

where the per-event average multiplicity squared is given by $N_{(2)}/\epsilon = \bar{N}^2$ for events with fixed multiplicity. Using the preceding sums, Eq. (20) can be rewritten as

$$\begin{aligned} \bar{\rho}'_{\text{BW,se}}(y_{t1}, y_{t2}) & = \frac{\bar{N} - 1}{\bar{N}} \sum_{\beta_1, \beta_2} \sum_{\eta_{t0_1}, \eta_{t0_2}} \frac{N_{(2)}}{\epsilon} \frac{N_{\beta_1\beta_2}}{N_{(2)}} \\ & \times \frac{N_{\beta_1\eta_{t0_1}\beta_2\eta_{t0_2}}}{N_{\beta_1\beta_2}} \frac{\sum_{j=1}^{\epsilon} \rho_{\text{BW},j\beta_1\eta_{t0_1}}(y_{t1}) \rho_{\text{BW},j\beta_2\eta_{t0_2}}(y_{t2})}{N_{\beta_1\eta_{t0_1}\beta_2\eta_{t0_2}}} \\ & = \frac{\bar{N} - 1}{\bar{N}} \sum_{\beta_1, \beta_2} \sum_{\eta_{t0_1}, \eta_{t0_2}} \frac{N_{(2)}}{\epsilon} \frac{N_{\beta_1\beta_2}}{N_{(2)}} \\ & \times \frac{N_{\beta_1\eta_{t0_1}\beta_2\eta_{t0_2}}}{N_{\beta_1\beta_2}} \hat{\rho}_{\text{BW},\beta_1\eta_{t0_1}}(y_{t1}) \hat{\rho}_{\text{BW},\beta_2\eta_{t0_2}}(y_{t2}), \end{aligned} \quad (24)$$

where the unit-normalized distributions introduced in Eq. (12) are included in the last line.

Ratio $N_{\beta_1\beta_2}/N_{(2)}$ is the probability for an arbitrary particle-pair to be emitted from two regions with binned inverse temperatures β_1 and β_2 . If there are no correlations among the β -emissions then we may again select gamma distributions [Eq. (13)] for both particles such that the probability is the integral over the bin of the

probability densities, given by

$$\begin{aligned} \frac{N_{\beta_1\beta_2}}{N_{(2)}} & = \int \int_{(\beta_1, \beta_2) \text{ bin}} d\beta_1 d\beta_2 f_{\gamma}(\beta_1, \bar{\beta}, q_{\beta}) f_{\gamma}(\beta_2, \bar{\beta}, q_{\beta}) \\ & = \int \int_{(\beta_1, \beta_2) \text{ bin}} d\beta_1 d\beta_2 f_{\gamma}(\beta_{\Sigma}, 2\bar{\beta}, 2q_{\beta}) \tilde{f}(\beta_{\Sigma}, \beta_{\Delta}, q_{\beta}). \end{aligned} \quad (25)$$

The transformation to sum and difference variables was explained in Ref. [14], where in Eq. (25) $\beta_{\Sigma} = \beta_1 + \beta_2$, and $\beta_{\Delta} = \beta_1 - \beta_2$. Probability density \tilde{f} is given by

$$\tilde{f}(\beta_{\Sigma}, \beta_{\Delta}, q_{\beta}) = \frac{\Gamma(2q_{\beta})}{\Gamma(q_{\beta})^2} \frac{1}{2^{2(q_{\beta}-1)}} \frac{1}{\beta_{\Sigma}} \left(1 - \frac{\beta_{\Delta}^2}{\beta_{\Sigma}^2}\right)^{q_{\beta}-1} \quad (26)$$

where Γ is the gamma function. Correlated β -emission is introduced by allowing the relative variances along the β_{Σ} and β_{Δ} directions to independently vary. We therefore redefine the ratio in Eq. (25) as

$$\frac{N_{\beta_1\beta_2}}{N_{(2)}} = \int \int_{(\beta_1, \beta_2) \text{ bin}} d\beta_1 d\beta_2 f_{\gamma}(\beta_{\Sigma}, 2\bar{\beta}, 2q_{\beta_{\Sigma}}) \tilde{f}(\beta_{\Sigma}, \beta_{\Delta}, q_{\beta_{\Delta}}) \quad (27)$$

where the changes in relative variances along the β_{Σ} and β_{Δ} directions are defined by parameters $\Delta(1/q)_{\Sigma}$ and $\Delta(1/q)_{\Delta}$, respectively, where

$$\begin{aligned} \Delta(1/q)_{\Sigma} & = 1/q_{\beta_{\Sigma}} - 1/q_{\beta} \\ \Delta(1/q)_{\Delta} & = 1/q_{\beta_{\Delta}} - 1/q_{\beta}. \end{aligned} \quad (28)$$

If $\Delta(1/q)_{\Sigma} > \Delta(1/q)_{\Delta}$, then the β emissions are correlated and if $\Delta(1/q)_{\Sigma} < \Delta(1/q)_{\Delta}$, then they are anti-correlated. Fitting is done using the combinations

$$\begin{aligned} \Delta(1/q)_1 & = [\Delta(1/q)_{\Sigma} + \Delta(1/q)_{\Delta}]/2 \\ \Delta(1/q)_2 & = [\Delta(1/q)_{\Sigma} - \Delta(1/q)_{\Delta}]/2, \end{aligned} \quad (29)$$

where $\Delta(1/q)_1$ measures the overall change in β -emission variance and $\Delta(1/q)_2$ measures the covariance.

Neglecting possible β, η_{t0} correlations in the emission source, as in the preceding subsection, quantity $N_{\beta_1\eta_{t0_1}\beta_2\eta_{t0_2}}/N_{\beta_1\beta_2}$ can be approximated by $N_{\eta_{t0_1}\eta_{t0_2}}/N_{(2)}$ in Eq. (24). If there are no correlations among the fluctuations in transverse flow then we may write

$$\begin{aligned} \frac{N_{\eta_{t0_1}\eta_{t0_2}}}{N_{(2)}} & = \\ & \int \int_{(\eta_{t0_1}, \eta_{t0_2}) \text{ bin}} d\eta_{t0_1} d\eta_{t0_2} g(\eta_{t0_1}, \bar{\eta}_{t0}, \sigma_{\eta_t}) g(\eta_{t0_2}, \bar{\eta}_{t0}, \sigma_{\eta_t}) \end{aligned} \quad (30)$$

using Eq. (15). When correlations are allowed Eq. (30) becomes

$$\begin{aligned} \frac{N_{\eta_{t0_1}\eta_{t0_2}}}{N_{(2)}} &= \iint_{(\eta_{t0_1}, \eta_{t0_2})_{\text{bin}}} d\eta_{t0_1} d\eta_{t0_2} g_2(\eta_{t0_1}, \eta_{t0_2}, \bar{\eta}_{t0}, \sigma_{\eta_{t\Sigma}}, \sigma_{\eta_{t\Delta}}) \\ &= \iint_{(\eta_{t0_1}, \eta_{t0_2})_{\text{bin}}} d\eta_{t0_1} d\eta_{t0_2} \mathcal{N}_{g_2} \eta_{t0_1} \eta_{t0_2} \exp \left\{ -\frac{1}{2} \left[\left(\frac{\eta_{t0_\Sigma} - 2\bar{\eta}_{t0}}{\sqrt{2}\sigma_{\eta_{t\Sigma}}} \right)^2 + \left(\frac{\eta_{t0_\Delta}}{\sqrt{2}\sigma_{\eta_{t\Delta}}} \right)^2 \right] \right\}, \end{aligned} \quad (31)$$

where $\eta_{t0_{\Sigma,\Delta}} = \eta_{t0_1} \pm \eta_{t0_2}$, $\eta_{t0_{1,2}} = (\eta_{t0_\Sigma} \pm \eta_{t0_\Delta})/2$, \mathcal{N}_{g_2} normalizes the 2D distribution to unity, and the widths are defined as

$$\sigma_{\eta_{t\Sigma}} \equiv \sigma_{\eta_t} + \Delta_{\eta_t}/2, \quad \sigma_{\eta_{t\Delta}} \equiv \sigma_{\eta_t} - \Delta_{\eta_t}/2. \quad (32)$$

Combining factors from Eqs. (27), (31) and (17) in Eq. (24), and taking the continuum limit, gives the 4D integration result

$$\begin{aligned} \bar{\rho}'_{\text{BW,se}}(y_{t1}, y_{t2}) &= \bar{N}(\bar{N} - 1) \iint d\beta_1 d\beta_2 f_\gamma(\beta_\Sigma, 2\bar{\beta}, 2q_{\beta_\Sigma}) \tilde{f}(\beta_\Sigma, \beta_\Delta, q_{\beta_\Delta}) \iint d\eta_{t0_1} d\eta_{t0_2} g_2(\eta_{t0_1}, \eta_{t0_2}, \bar{\eta}_{t0}, \sigma_{\eta_{t\Sigma}}, \sigma_{\eta_{t\Delta}}) \\ &\times \hat{\rho}_{\text{BW},\beta_1\eta_{t0_1}}(y_{t1}) \hat{\rho}_{\text{BW},\beta_2\eta_{t0_2}}(y_{t2}). \end{aligned} \quad (33)$$

The same numerical integration ranges and step sizes used for the single-particle BW calculation were used in the numerical integration in Eq. (33).

C. Two-particle correlation

By definition, the two-particle correlations contained in the two-particle, BW distribution in Eq. (33) equal the difference between it and the product of marginals, where

$$\bar{\rho}_{\text{BW,marg}}(y_{t1}) \equiv \frac{1}{\bar{N} - 1} \sum_{y_{t2}} \bar{\rho}'_{\text{BW,se}}(y_{t1}, y_{t2}) \quad (34)$$

with normalization $\sum_{y_{t1}} \bar{\rho}_{\text{BW,marg}}(y_{t1}) = \bar{N}$. To ensure consistency with the single-particle measurements we also require the marginal of the entire two-particle distribution in Eq. (19) to equal the measured charge

distribution $\bar{\rho}_{\text{ch}}(y_t)$ in Eq. (7). However, in order to fit the correlation data the variances in the inverse temperature and transverse flow rapidity, $\Delta(1/q)_{1,2}$ and Δ_{η_t} , were freely varied resulting in marginals which may not equal $\bar{\rho}_{\text{BW}}(y_t)$ in Eqs. (7) and (8). This condition requires an adjusted residual $\delta\bar{\rho}'(y_t)$ defined by

$$\delta\bar{\rho}'(y_t) \equiv \bar{\rho}_{\text{ch}}(y_t) - \bar{\rho}_{\text{BW,marg}}(y_t), \quad (35)$$

where $\sum_{y_t} \delta\bar{\rho}'(y_t) = 0$. Acceptable BW correlation model fits should not only describe the correlation data but should maintain a small residual such that $\delta\bar{\rho}'(y_t) \ll \bar{\rho}_{\text{ch}}(y_t)$.

The complete two-particle distribution, whose marginal equals the measured single-particle charge distribution, is therefore given by

$$\begin{aligned} \bar{\rho}_{\text{BW,se}}(y_{t1}, y_{t2}) &= \bar{\rho}'_{\text{BW,se}}(y_{t1}, y_{t2}) \\ &+ \frac{\bar{N} - 1}{\bar{N}} [\bar{\rho}_{\text{BW,marg}}(y_{t1}) \delta\bar{\rho}'(y_{t2}) + \bar{\rho}_{\text{BW,marg}}(y_{t2}) \delta\bar{\rho}'(y_{t1}) + \delta\bar{\rho}'(y_{t1}) \delta\bar{\rho}'(y_{t2})], \end{aligned} \quad (36)$$

where the pair normalization factor $(\bar{N} - 1)/\bar{N}$ from Eq. (19) was applied to the last three terms. The uncorrelated reference pair distribution is defined as the product of marginals given by

$$\begin{aligned} \bar{\rho}_{\text{BW,ref}}(y_{t1}, y_{t2}) &= \frac{\bar{N} - 1}{\bar{N}} [\bar{\rho}_{\text{BW,marg}}(y_{t1}) \bar{\rho}_{\text{BW,marg}}(y_{t2}) + \bar{\rho}_{\text{BW,marg}}(y_{t1}) \delta\bar{\rho}'(y_{t2}) + \bar{\rho}_{\text{BW,marg}}(y_{t2}) \delta\bar{\rho}'(y_{t1}) \\ &+ \delta\bar{\rho}'(y_{t1}) \delta\bar{\rho}'(y_{t2})] = \frac{\bar{N} - 1}{\bar{N}} \bar{\rho}_{\text{ch}}(y_{t1}) \bar{\rho}_{\text{ch}}(y_{t2}) \end{aligned} \quad (37)$$

where pair normalization factor $(\bar{N} - 1)/\bar{N}$ must also be applied to the reference as required by the $\Delta\sigma_{p_t:n}^2$ based derivation [24]. The per-pair normalized correlation is given by

$$\frac{\Delta\bar{\rho}_{\text{BW}}}{\bar{\rho}_{\text{BW,ref}}}(y_{t1}, y_{t2}) \equiv \frac{\bar{\rho}_{\text{BW,se}}(y_{t1}, y_{t2}) - \bar{\rho}_{\text{BW,ref}}(y_{t1}, y_{t2})}{\bar{\rho}_{\text{BW,ref}}(y_{t1}, y_{t2})} = \frac{\bar{\rho}'_{\text{BW,se}}(y_{t1}, y_{t2}) - \frac{\bar{N}-1}{\bar{N}} \bar{\rho}_{\text{BW,marg}}(y_{t1}) \bar{\rho}_{\text{BW,marg}}(y_{t2})}{\bar{\rho}_{\text{BW,ref}}(y_{t1}, y_{t2})}. \quad (38)$$

The final, BW correlation quantity to be compared to data includes a prefactor corresponding to that applied to the data [21]. In general, the purpose of a prefactor is to replace the pair ratio in Eq. (38), which is required in data analysis to correct for efficiency and acceptance, with a quantity better suited to the study of specific scaling trends, *e.g.* binary scaling, per-trigger scaling, etc. A prefactor may also be required by the specific charge-pair combinations used, and the relative pseudorapidity and/or azimuthal angle selections. For the present study we use a charge-independent (CI, all charge-pair combinations), away-side azimuth (AS, $|\phi_1 - \phi_2| > \pi/2$), soft-process particle production prefactor, $\mathcal{P}_{\text{Fac,soft}}^{\text{AS-CI}}(y_{t1}, y_{t2})$. The final correlation quantity is given by

$$\frac{\Delta \bar{\rho}_{\text{BW}}}{\sqrt{\bar{\rho}_{\text{soft}}}}(y_{t1}, y_{t2}) = \mathcal{P}_{\text{Fac,soft}}^{\text{AS-CI}}(y_{t1}, y_{t2}) \frac{\Delta \bar{\rho}_{\text{BW}}}{\bar{\rho}_{\text{BW,ref}}}(y_{t1}, y_{t2}) \quad (39)$$

where the prefactor is defined and calculated in the following.

In the present model the specific purposes of prefactor $\mathcal{P}_{\text{Fac,soft}}^{\text{AS-CI}}$ are three-fold: (1) To convert the number of correlated pairs per final-state *pair* quantity in Eq. (38) to a number of correlated pairs per final-state *particle* ratio as in Pearson's correlation coefficient definition [42]. The latter has the form of correlated pair number per geometric mean of the product of single-particle distributions [21]. (2) To scale this “pairs per singles” ratio to account for the fact that only one-half of the available charged-particle pairs are included when selecting only the away-side pairs whose relative azimuth angle $|\phi_1 - \phi_2|$ exceeds $\pi/2$. Away-side pairs were selected for the analytical model fitting in Ref. [20] in order to suppress contributions from HBT correlations [14]. (3) To provide an overall normalization which facilitates tests of binary scaling in the correlation structures. The last requirement can be achieved by using the soft QCD-process particle yield, as estimated in the Kharzeev-Nardi [30] two-component model, in the denominator on the left-hand-side of Eq. (39) given by $\sqrt{\bar{\rho}_{\text{soft}}(y_{t1}, y_{t2})}$. In the KN model soft-QCD yields are proportional to N_{part} , where N_{part} is the number of participant nucleons in the collision. If the number of correlated pairs in the numerator is proportional to the number of binary nucleon + nucleon (N+N) interactions, N_{bin} , then correlation quantity $\Delta \bar{\rho}_{\text{BW}}/\sqrt{\bar{\rho}_{\text{soft}}}$ in Eq. (39) will be proportional to $N_{\text{bin}}/N_{\text{part}}$. Ratio $N_{\text{bin}}/N_{\text{part}}$ is proportional to centrality measure $\nu \equiv N_{\text{bin}}/(N_{\text{part}}/2)$ [31] which enables a straightforward way to detect binary scaling in centrality dependent correlations by searching for correlation structures which linearly increase with centrality measure ν .

The soft-reference prefactor for away-side pairs and all charged particles is given by

$$\mathcal{P}_{\text{Fac,soft}}^{\text{AS-CI}} \equiv \frac{1}{\sqrt{2}} \frac{\frac{d^2 N_{\text{ch}}}{dy_{t1} d\eta_1} \frac{d^2 N_{\text{ch}}}{dy_{t2} d\eta_2}}{\left[\frac{d^2 N_{\text{ch,soft}}}{dy_{t1} d\eta_1} \frac{d^2 N_{\text{ch,soft}}}{dy_{t2} d\eta_2} \right]^{1/2}} \quad (40)$$

where the distributions are calculated at the mid-points of each y_t -bin. In this equation the charged particle distribution was parametrized with a Levy distribution where

$$\begin{aligned} \frac{d^2 N_{\text{ch}}}{dy_t d\eta} &= 2\pi p_t \frac{dp_t}{dy_t} \left[\frac{d^2 N_{\text{ch}}}{2\pi p_t dp_t d\eta} \right] \\ &= \frac{2\pi p_t m_t A_{\text{ch}}}{[1 + (m_t - m_0)/(T_{\text{ch}} q_{\text{ch}})]^{q_{\text{ch}}}}. \end{aligned} \quad (41)$$

Fit parameters A_{ch} , T_{ch} and q_{ch} for the 200 GeV Au+Au spectra data reported by the STAR Collaboration [39] were determined in the y_t range from 1.34 to 4.36, corresponding to $p_t \in [0.25, 5.5]$ GeV/c, and are listed in Table II. The N_{part} scaling, Kharzeev and Nardi soft-QCD process spectrum was also parametrized with the Levy distribution and is given by,

$$\frac{d^2 N_{\text{ch,soft}}}{dy_t d\eta} = \frac{2\pi p_t m_t A_{\text{soft}} (N_{\text{part}}/2)}{[1 + (m_t - m_0)/(T_{\text{soft}} q_{\text{soft}})]^{q_{\text{soft}}}}. \quad (42)$$

The number of participants for 200 GeV Au+Au minimum-bias collisions was estimated in Ref. [31] and interpolated to the present centrality bins (see Table II). A method for estimating the N_{part} scaling, soft-QCD process spectrum was presented in Ref. [43]. In the present analysis the soft-QCD distribution was estimated by extrapolating the STAR [39] and PHENIX [44] Collaborations' p_t spectra data in each p_t bin to the N+N collision limit and fitting the resulting distribution with the Levy model in Eq. (42). The resulting fits gave $A_{\text{soft}} = 5.81$ (c/GeV²), $T_{\text{soft}} = 0.169$ GeV, and $q_{\text{soft}} = 13.8$.

TABLE II: Levy model fit parameters to the STAR Collaboration 200 GeV Au+Au minimum-bias charged particle p_t spectra data in Ref. [39] in the range $y_t \in [1.34, 4.36]$. Also listed are the number of participant nucleons, number of binary N+N collisions, and centrality measure ν [31]. The estimated soft-process p_t spectrum Levy model parameters in Eq. (42) are: $A_{\text{soft}} = 5.81$ (c/GeV²), $T_{\text{soft}} = 0.169$ GeV, and $q_{\text{soft}} = 13.8$.

Centrality (%)	ν	N_{part}	N_{bin}	A_{ch} (c/GeV ²)	T_{ch} (GeV)	q_{ch}
0-5	5.95	350.3	1042	1154.8	0.2176	17.41
5-10	5.50	299.5	824	935.8	0.2167	17.15
10-20	4.98	233.7	582	724.2	0.2129	16.00
20-30	4.34	166.4	361	503.4	0.2090	15.09
30-40	3.75	116.1	218	350.3	0.2036	14.28
40-60	2.87	59.8	85.7	205.76	0.1882	12.49
60-80	1.97	19.5	19.2	77.96	0.1695	11.06

III. TWO-COMPONENT FRAGMENTATION MODEL WITH FLUCTUATIONS

A. Single-particle distribution

The two-component fragmentation model presented here is based on the two-component multiplicity produc-

tion model of Kharzeev and Nardi [30], discussed briefly in the preceding section, which assumes that particle production is dominated by two processes which scale either with N_{part} or N_{bin} . The relevance of this model in the description of the peaked correlation structures on (p_{t1}, p_{t2}) from p+p collisions was discussed in Ref. [15]. In this model the particle yield N in some (η, ϕ) acceptance is given by

$$N = n_{pp}(1-x)N_{\text{part}}/2 + n_{pp}xN_{\text{bin}} \quad (43)$$

where $n_{pp} = 4.95$ is the charged-particle yield in $\sqrt{s} = 200$ GeV non-singly diffractive, minimum-bias p+p collisions at mid-rapidity within acceptance $\Delta\eta = 2$, full 2π azimuth and $p_t > 0.15$ GeV/c [43]. Parameter x is approximately 0.1 [43] for charged-particle production in $\sqrt{s_{\text{NN}}} = 200$ GeV minimum-bias Au+Au collisions within the same acceptance. In the present application we assume the N_{part} -scaling production derives from soft-QCD, longitudinal fragmentation of color-flux tubes [26], or “color-strings” as parametrized for example in the LUND model [1]. Similarly, the N_{bin} -scaling production corresponds to semi-hard (few GeV) and hard (few tens of GeV) QCD, transversely fragmenting partons, or jets, as described in PYTHIA [2]. For the present application the N_{bin} -scaling production is dominated by the lower energy, semi-hard part of the spectrum. Furthermore, we allow fluctuations in the following: (1) the p_t -distribution shape, *e.g.* overall slope parameter β for the charged-particle production from each longitudinally fragmenting color-string [1, 26]; (2) the energy of each semi-hard parton scattering and resulting jet; (3) the event-wise relative number of “soft” and “semi-hard” QCD process particles produced.

For a collection of collision events within a centrality bin, the event-average soft-process component is calculated similarly to the preceding blast-wave model where

$$\bar{\rho}_s(y_t) = \frac{1}{\epsilon} \sum_{j=1}^{\epsilon} \rho_{s,j}(y_t) = \sum_{\beta} \frac{1}{\epsilon} \sum_{j=1}^{\epsilon} \rho_{s,j\beta}(y_t) \quad (44)$$

and $\rho_{s,j\beta}(y_t)$ is the number of charged particles in a y_t -bin in event j which were emitted from longitudinally fragmenting color-strings characterized by binned p_t -slope parameter β . In analogy with Eqs. (9)-(11) we define the total number of particles in transverse rapidity bin y_t emitted from color-strings with p_t -slope β , the total number of these particles for all considered y_t , and the total number of emitted particles from all color-strings as follows:

$$N_{s\beta}(y_t) \equiv \sum_{j=1}^{\epsilon} \rho_{s,j\beta}(y_t), \quad (45)$$

$$N_{s\beta} \equiv \sum_{y_t} N_{s\beta}(y_t), \quad (46)$$

$$N_s \equiv \sum_{\beta} N_{s\beta}. \quad (47)$$

The event-average soft-process component yield in each y_t -bin is given by

$$\bar{\rho}_s(y_t) = \sum_{\beta} \frac{N_s}{\epsilon} \frac{N_{s\beta}}{N_s} \frac{N_{s\beta}(y_t)}{N_{s\beta}} = \bar{N}_s \sum_{\beta} f_{\beta} \hat{\rho}_{s,\beta}(y_t), \quad (48)$$

where $\bar{N}_s = N_s/\epsilon$, $f_{\beta} = N_{s\beta}/N_s$, and unit-normal distribution $\hat{\rho}_{s,\beta}(y_t)$ is $N_{s\beta}(y_t)/N_{s\beta}$. As in the preceding sections the right-hand side of Eq. (48) is calculated in the continuum limit, given by

$$\bar{\rho}_s(y_t) = \bar{N}_s \int d\beta f(\beta, \bar{\beta}, q_{\beta}) \hat{\rho}_{s,\beta}(y_t) \quad (49)$$

where $f(\beta, \bar{\beta}, q_{\beta})$ is again assumed to be the gamma-distribution in Eq. (13) and $\hat{\rho}_{s,\beta}(y_t)$ is proportional to a Maxwell-Boltzmann distribution $\exp[-\beta(m_t - m_0)]$. Quantities in Eq. (49) are calculated at the mid-points of the y_t bins as usual. The integral in Eq. (49) results in the Levy distribution given in Eq. (14), where $\bar{\rho}_s(y_t)$ is determined by the soft production spectrum estimated in Eq. (42) and is given by

$$\bar{\rho}_s(y_t) = \Delta\eta\epsilon_{y_t} \frac{d^2 N_{\text{ch,soft}}}{dy_t d\eta}. \quad (50)$$

The mean, soft-process produced multiplicity, \bar{N}_s , is the total yield of $\bar{\rho}_s(y_t)$ summed over the y_t acceptance.

The transverse fragmentation, “semi-hard” QCD process particle yield is similarly given by

$$\bar{\rho}_h(y_t) = \frac{1}{\epsilon} \sum_{j=1}^{\epsilon} \rho_{h,j}(y_t) = \sum_{y_{\text{max}}} \frac{1}{\epsilon} \sum_{j=1}^{\epsilon} \rho_{h,jy_{\text{max}}}(y_t) \quad (51)$$

where the jet energy-dependence is accounted for via the maximum possible transverse rapidity of the particle fragments, y_{max} . Distribution $\rho_{h,jy_{\text{max}}}(y_t)$ is the number of accepted charged particles in event j , in the transverse rapidity bin at y_t , from jets whose energy is characterized by binned quantity y_{max} with bin width $\epsilon_{y_{\text{max}}}$. Defining the total semi-hard process multiplicity in an arbitrary y_t bin from all the jets with y_{max} , and the corresponding sums over y_t bins and y_{max} as

$$N_{hy_{\text{max}}}(y_t) \equiv \sum_{j=1}^{\epsilon} \rho_{h,jy_{\text{max}}}(y_t), \quad (52)$$

$$N_{hy_{\text{max}}} \equiv \sum_{y_t} N_{hy_{\text{max}}}(y_t), \quad (53)$$

$$N_h \equiv \sum_{y_{\text{max}}} N_{hy_{\text{max}}}, \quad (54)$$

respectively, yields the result

$$\bar{\rho}_h(y_t) = \sum_{y_{\text{max}}} \frac{N_h}{\epsilon} \frac{N_{hy_{\text{max}}}}{N_h} \frac{N_{hy_{\text{max}}}(y_t)}{N_{hy_{\text{max}}}}. \quad (55)$$

The last ratio on the right-hand side of this equation is defined as

$$\hat{\rho}_{h,y_{\max}}(y_t) \equiv N_{h,y_{\max}}(y_t)/N_{h,y_{\max}}, \quad (56)$$

which is the fraction of particles produced in an arbitrary y_t bin by jets with y_{\max} . The second ratio,

$$\hat{g}_{y_{\max}} \equiv \frac{N_{h,y_{\max}}}{N_h}, \quad (57)$$

is the fraction of semi-hard process produced particles which fragmented from jets with characteristic energy parameter y_{\max} . The average number of semi-hard particles per event is $\bar{N}_h = N_h/\epsilon$. The latter is defined to be the difference between the average charged and soft-process produced particle multiplicities within the acceptance. Substituting the above into Eq. (55) and taking the continuum limit give

$$\begin{aligned} \bar{\rho}_h(y_t) &= \bar{N}_h \sum_{y_{\max}} \hat{g}_{y_{\max}} \hat{\rho}_{h,y_{\max}}(y_t) \\ &\rightarrow \bar{N}_h \int_0^\infty dy_{\max} \hat{g}(y_{\max}) \hat{\rho}_{h,y_{\max}}(y_t) \\ &\equiv \bar{\rho}_{\text{Jet}[g]}(y_t), \end{aligned} \quad (58)$$

where the subscript notation in the final quantity denotes the convolution integral for distribution $\hat{g}(y_{\max})$.

Quantity $\hat{g}(y_{\max})$ is the probability distribution for producing particles from a jet with maximum fragment rapidity y_{\max} in a N+N collision. In Ref. [3] this quantity is given by a QCD power-law distribution with low momentum cut-off, multiplied by a quadratic yield increase factor $(y_{\max} - y_{\min})^2$ where y_{\min} is an empirical

parameter. The quadratically increasing yield results from the approximate shape invariant evolution of the beta distribution of jet fragments observed at LEP in $e^+ + e^- \rightarrow \text{jet}(Q^2) + X$ production over a wide range of jet energies [3, 45]. Probability distribution $\hat{g}(y_{\max})$ is proportional to a QCD power-law with low momentum cut-off given by [3]

$$\begin{aligned} \hat{g}(y_{\max}) &\propto \\ &\frac{1}{2} \sigma_{\text{dijet}} (n_{\text{QCD}} - 2) \left\{ \tanh \left(\frac{y_{\max} - y_{\text{cut}}}{\xi_{\text{cut}}} \right) + 1 \right\} \\ &\times e^{-(n_{\text{QCD}}-2)(y_{\max}-y_{\text{cut}})} (y_{\max} - y_{\min})^2, \end{aligned} \quad (59)$$

where $\sigma_{\text{dijet}} = 2.5$ mb at $\sqrt{s} = 200$ GeV, and from Ref. [3] low momentum cut-off parameters are $y_{\text{cut}} = 3.75$ and $\xi_{\text{cut}} = 0.1$, $n_{\text{QCD}} = 7.5$ and $y_{\min} = 0.35$.

Particle distribution $\hat{\rho}_{h,y_{\max}}(y_t)$ is proportional to the distribution deduced in Ref. [3] for $e^+ + e^- \rightarrow \text{jet} + X$ multiplied by a low momentum jet-fragment suppression factor determined by analyzing the jet fragment distributions from $p + \bar{p} \rightarrow \text{jet} + X$ collisions [46]. Quantity $\hat{\rho}_{h,y_{\max}}(y_t)$ from Ref. [3] is proportional to

$$\hat{\rho}_{h,y_{\max}}(y_t) \propto \tanh \left(\frac{y_t - y_0}{\xi_y} \right) \frac{u^{p-1} (1-u)^{q-1}}{B(p, q)} \quad (60)$$

for $y_{\max} \geq y_t \geq y_0$, where the last factor is a normalized beta distribution with

$$u \equiv \frac{y_t - y_{\min}}{y_{\max} - y_{\min}}, \quad \in [0, 1]. \quad (61)$$

Quantity $B(p, q) = \Gamma(p)\Gamma(q)/\Gamma(p+q)$ where Γ is the gamma function.

Collecting terms, the above semi-hard process particle distribution becomes

$$\begin{aligned} \bar{\rho}_{\text{Jet}[g]}(y_t) &= \bar{N}_h \mathcal{N}_h \int_0^\infty dy_{\max} \frac{1}{2} \sigma_{\text{dijet}} (n_{\text{QCD}} - 2) \left\{ \tanh \left(\frac{y_{\max} - y_{\text{cut}}}{\xi_{\text{cut}}} \right) + 1 \right\} \\ &\times e^{-(n_{\text{QCD}}-2)(y_{\max}-y_{\text{cut}})} (y_{\max} - y_{\min})^2 \tanh \left(\frac{y_t - y_0}{\xi_y} \right) \Big|_{y_t \geq y_0} \frac{u^{p-1} (1-u)^{q-1}}{B(p, q)} \Big|_{y_{\min} \leq y_t \leq y_{\max}} \end{aligned} \quad (62)$$

where \mathcal{N}_h normalizes the sum of $\bar{\rho}_{\text{Jet}[g]}(y_t)$ over all y_t bins to \bar{N}_h ; quantities in Eq. (62) are calculated at the mid-points of the y_t bins. Combining the contributions in Eqs. (50) and (62) the charged-particle distribution in this model is defined as

$$\bar{\rho}_{\text{ch}}(y_t) = \bar{\rho}_s(y_t) + \bar{\rho}_{\text{Jet}[g]}(y_t) + \delta\bar{\rho}(y_t) \quad (63)$$

where $\delta\bar{\rho}(y_t)$ is the residual between the model components and data.

The two-component fragmentation model was applied to the charged-particle p_t spectrum data discussed in Sec. II. The semi-hard process particle production model in Eq. (62) was fitted to the difference distribution $\bar{\rho}_{\text{ch}}(y_t) - \bar{\rho}_s(y_t)$ in the y_t range from 1.34 to 4.36, corresponding to p_t from 0.25 to 5.5 GeV/c, by varying essen-

tially all the parameters including n_{QCD} , the jet production cut-off y_{cut} , the soft-fragment cut-off $y_0 = \xi_y$, and fragment distribution parameters p and q in Eq. (60). Better fits were achieved by variation of the shape of the fragment distribution, via parameters p and q , than were obtained from the cut-off parameter y_0 ; the latter was

subsequently set to zero.

Best fits were attained via χ^2 -minimization. Quantitative descriptions of the semi-hard component spectrum at the maximum peak and in the higher momentum tails were achieved for each centrality. Example fits to $\bar{\rho}_{\text{ch}}(y_t)$ are shown in Fig. 2 for the 60-80%, 20-30% and 0-5% centralities. The TCF model parameters are listed for all centralities in Table III. Parameter n_{QCD} increases slightly and smoothly with centrality, increasing above the value (7.5) estimated in Ref. [3]. Jet production cut-off parameter y_{cut} is approximately constant and larger than the value (3.75) in Ref. [3]. The modifications of the fragment distribution relative to the nominal shape from Ref. [3] are also shown in the lower row of panels. The trends imply a softening of the fragment distribution (suppression at higher p_t) coupled with a lower-momentum suppression relative to that observed in $e^+ + e^- \rightarrow \text{jet} + X$, discussed in Ref. [3], which quickly develops with increasing collision centrality. The residuals vary from $\leq 2\%$ to $\leq 4\%$ of the charged-particle distribution from peripheral to most-central collisions, respectively, for $y_t < 3$. The residuals increase in relative magnitude at larger $y_t > 3$, varying from $\leq 3\%$ to $\leq 7\%$ of the charged-particle distribution from peripheral to most-central collisions, respectively.

TABLE III: TCF model fit parameters for the 200 GeV Au+Au minimum-bias p_t spectra data from STAR [39]. Data were fit in the y_t range from 1.34 to 4.36 using 30 data points at each centrality. Fit quality was insensitive to soft-fragment cut-off parameter y_0 which was subsequently set to zero.

Centrality(%)	\bar{N}_s	\bar{N}_h	n_{QCD}	y_{cut}	p	q	χ^2/DoF
0-5	649.2	479.5	9.1	4.3	5.6	6.9	1.632
5-10	555.1	354.9	9.0	4.3	5.9	7.0	1.823
10-20	433.1	256.7	8.55	4.35	5.95	7.3	1.042
20-30	308.4	160.0	8.35	4.4	6.2	7.6	0.957
30-40	215.2	98.8	8.1	4.45	6.25	7.85	1.266
40-60	110.8	53.4	7.6	4.3	4.7	6.4	0.665
60-80	36.1	16.6	7.15	4.25	3.5	5.7	0.410

B. Two-particle distribution

In the two-component fragmentation model the two-particle distribution is generated by emissions from multiple color-strings and from multiple transversely fragmenting partons (jets) in each heavy-ion collision. These processes are characterized by p_t slope parameters β_1 and β_2 and by jet parameters y_{max_1} and y_{max_2} for arbitrary particles 1 and 2, respectively. Correlations arise when the event-average probability distributions on (β_1, β_2) and $(y_{\text{max}_1}, y_{\text{max}_2})$ are correlated. In the present application correlated fluctuations between color-string β and jet y_{max} are not included as these are defined to be independent processes in this model. The two-particle

same-event pair-distribution in this model is given by

$$\begin{aligned} \bar{\rho}_{\text{TCF,se}}(y_{t1}, y_{t2}) = & \frac{\bar{N} - 1}{\bar{N}} \frac{1}{\epsilon} \sum_{j=1}^{\epsilon} [\rho_{s,j}(y_{t1}) + \rho_{h,j}(y_{t1}) + \delta\bar{\rho}(y_{t1})] \\ & \times [\rho_{s,j}(y_{t2}) + \rho_{h,j}(y_{t2}) + \delta\bar{\rho}(y_{t2})]. \end{aligned} \quad (64)$$

The “string-string” term can be expanded as a sum over correlated, binned p_t slope parameters (β_1, β_2) , where

$$\begin{aligned} \bar{\rho}_{ss} & \equiv \frac{\bar{N} - 1}{\bar{N}} \frac{1}{\epsilon} \sum_{j=1}^{\epsilon} \rho_{s,j}(y_{t1}) \rho_{s,j}(y_{t2}) \\ & = \frac{\bar{N} - 1}{\bar{N}} \sum_{\beta_1, \beta_2} \frac{1}{\epsilon} \sum_{j=1}^{\epsilon} \rho_{s,j\beta_1}(y_{t1}) \rho_{s,j\beta_2}(y_{t2}). \end{aligned} \quad (65)$$

Defining pair sums as before yields

$$N_{s\beta_1\beta_2}(y_{t1}, y_{t2}) \equiv \sum_{j=1}^{\epsilon} \rho_{s,j\beta_1}(y_{t1}) \rho_{s,j\beta_2}(y_{t2}), \quad (66)$$

$$N_{s\beta_1\beta_2} \equiv \sum_{y_{t1}, y_{t2}} N_{s\beta_1\beta_2}(y_{t1}, y_{t2}), \quad (67)$$

$$N_{(2)s} \equiv \sum_{\beta_1, \beta_2} N_{s\beta_1\beta_2}, \quad (68)$$

which gives the “string-string” term as

$$\bar{\rho}_{ss} = \frac{\bar{N} - 1}{\bar{N}} \sum_{\beta_1, \beta_2} \frac{N_{(2)s}}{\epsilon} \frac{N_{s\beta_1\beta_2}}{N_{(2)s}} \frac{N_{s\beta_1\beta_2}(y_{t1}, y_{t2})}{N_{s\beta_1\beta_2}}. \quad (69)$$

The last term in this equation represents the unit-normalized pair distribution analogous to Eqs. (24), (48) and (49). It is given by

$$\begin{aligned} \frac{N_{s\beta_1\beta_2}(y_{t1}, y_{t2})}{N_{s\beta_1\beta_2}} = & \mathcal{N}_s \mathcal{J} \int \int_{(\beta_1, \beta_2) \text{ bin}} d\beta_1 d\beta_2 e^{-\beta_1(m_{t1}-m_0)} e^{-\beta_2(m_{t2}-m_0)}, \end{aligned} \quad (70)$$

where \mathcal{N}_s is a normalization factor and $\mathcal{J} = 4\pi^2 p_{t1} m_{t1} p_{t2} m_{t2}$ is the Jacobian which transforms the distributions on transverse mass to distributions on transverse rapidity. The second term is the correlated p_t slope parameter distribution given by

$$\frac{N_{s\beta_1\beta_2}}{N_{(2)s}} = \int \int_{(\beta_1, \beta_2) \text{ bin}} d\beta_1 d\beta_2 f_{\gamma}(\beta_{\Sigma}, 2\bar{\beta}, 2q_{\beta_{\Sigma}}) \tilde{f}(\beta_{\Sigma}, \beta_{\Delta}, q_{\beta_{\Delta}}) \quad (71)$$

as in Eq. (27), and the first term is the average number of pairs from color-string fragmentation, given by

$$N_{(2)s}/\epsilon = \bar{N}_s^2 + \sigma_0^2 \quad (72)$$

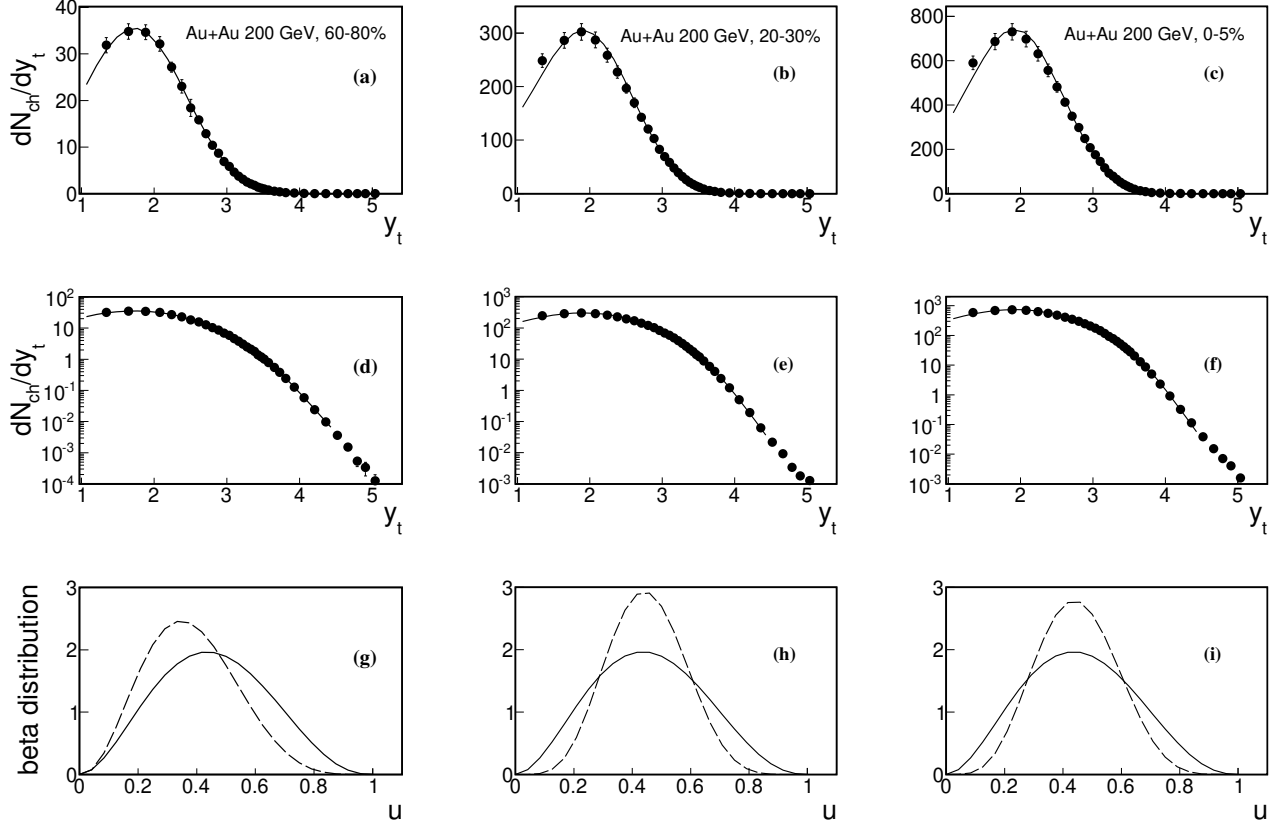


FIG. 2: Fluctuating TCF model fits to the 200 GeV Au+Au minimum-bias p_t spectrum data from STAR [39] (see text) showing only the 60-80%, 20-30% and 0-5% centrality results. Combined soft plus semi-hard process yields are shown as quantity dN_{ch}/dy_t versus transverse rapidity y_t , assuming pseudorapidity acceptance $\Delta\eta = 2$. Linear (upper row) and semi-log (middle row) plots are shown for the same data and model fits to allow visual access to the fit quality in both the lower and higher y_t ranges. Modifications to the universal fragment distribution for each centrality are shown in the lower row of panels where the nominal (solid lines) [3] and fitted (dashed lines) normalized beta distributions are plotted versus transverse rapidity scaling variable u in Eq. (61).

where σ_0^2 is the variance of the event-wise fluctuation in the number of particles emitted by color-string fragmentation. Taking the continuum limit for the β_1, β_2 summations in Eq. (69) and using the integration result in Ref. [14] give

$$\begin{aligned} \bar{\rho}_{ss} &= \frac{\bar{N}-1}{\bar{N}} (\bar{N}_s^2 + \sigma_0^2) \mathcal{N}_{ss} \mathcal{J} \left(1 + \frac{\bar{\beta} m_{t\Sigma}}{2q\beta_\Sigma} \right)^{-2q\beta_\Sigma} \\ &\times \left[1 - \left(\frac{\bar{\beta} m_{t\Delta}}{2q\beta_\Delta + \bar{\beta} m_{t\Sigma}} \right)^2 \right]^{-q\beta_\Delta} \\ &\equiv \frac{\bar{N}-1}{\bar{N}} (\bar{N}_s^2 + \sigma_0^2) \hat{\rho}_{2D-Levy}(y_{t1}, y_{t2}). \end{aligned} \quad (73)$$

The unit-normalized 2D Levy distribution is defined in the last line of Eq. (73) which was calculated at the mid-points of the y_t bins. Also in the preceding equation kinematic variables $m_{t\Sigma} = m_{t1} + m_{t2} - 2m_0$ and $m_{t\Delta} = m_{t1} - m_{t2}$ were introduced as well as fit parameters $\Delta(1/q)_{\Sigma, \Delta}$ and $\Delta(1/q)_{1,2}$ which are defined in analogy to those in Eqs. (28) and (29).

The “jet-jet” contribution, $\bar{\rho}_{hh}$, using the summation in Eq. (51) and introducing pair sums analogous to those in Eqs. (66)-(68), is given by

$$\begin{aligned} \bar{\rho}_{hh} &\equiv \frac{\bar{N}-1}{\bar{N}} \frac{1}{\epsilon} \sum_{j=1}^{\epsilon} \rho_{h,j}(y_{t1}) \rho_{h,j}(y_{t2}) \\ &= \frac{\bar{N}-1}{\bar{N}\epsilon} \sum_{y_{\max 1}, y_{\max 2}} \sum_{j=1}^{\epsilon} \rho_{h,j y_{\max 1}}(y_{t1}) \rho_{h,j y_{\max 2}}(y_{t2}) \\ &= \frac{\bar{N}-1}{\bar{N}} \sum_{y_{\max 1}, y_{\max 2}} \frac{N_{(2)h}}{\epsilon} \frac{N_{h y_{\max 1}, y_{\max 2}}}{N_{(2)h}} \\ &\times \frac{N_{h y_{\max 1}, y_{\max 2}}(y_{t1}, y_{t2})}{N_{h y_{\max 1}, y_{\max 2}}}. \end{aligned} \quad (74)$$

The unit-normalized pair distribution, correlated jet y_{\max} distribution, and average number of pairs from jet frag-

mentation are given respectively by

$$\frac{N_{hy_{\max_1}, y_{\max_2}}(y_{t1}, y_{t2})}{N_{hy_{\max_1}, y_{\max_2}}} = \hat{\rho}_{h, y_{\max_1}}(y_{t1}) \hat{\rho}_{h, y_{\max_2}}(y_{t2}), \quad (75)$$

where $\hat{\rho}_{h, y_{\max}}(y_t)$ is given in Eq. (60),

$$\frac{N_{hy_{\max_1}, y_{\max_2}}}{N_{(2)h}} = \iint_{(y_{\max_1}, y_{\max_2}) \text{ bin}} dy_{\max_1} dy_{\max_2} \hat{g}_2(y_{\max_1}, y_{\max_2}), \quad (76)$$

where \hat{g}_2 is defined below, and

$$N_{(2)h}/\epsilon = \bar{N}_h^2 + \sigma_0^2. \quad (77)$$

For the correlated distribution $\hat{g}_2(y_{\max_1}, y_{\max_2})$, a simplified functional definition was assumed in order to reduce the computational demands. The function combines an uncorrelated component and a fully correlated component given by

$$\hat{g}_2(y_{\max_1}, y_{\max_2}) = (1 - \gamma) \hat{h}(y_{\max_1}) \hat{h}(y_{\max_2}) + \gamma \hat{p}(y_{\max_1}) \delta(y_{\max_1} - y_{\max_2}), \quad (78)$$

where δ is the Dirac delta-function,

$$\hat{p}(y_{\max_1}) = \lim_{y_{\max_1} \rightarrow y_{\max_2}} \hat{g}'(y_{\max_1}) \hat{g}'(y_{\max_2}), \quad (79)$$

and $\hat{g}'(y_{\max})$ has the same form as $\hat{g}(y_{\max})$ in Eq. (59), but may have different parameter values. In taking the limit in the above equation the product of the two hyperbolic tangent cut-off functions in both instances of \hat{g}'

is approximated by a single cut-off function with variable parameter y_{cut}^* . In addition, exponential argument $2(n_{\text{QCD}} - 2)(y_{\max} - y_{\text{cut}})$ is written as $(n_{\text{QCD}}^* - 2)(y_{\max} - y_{\text{cut}}^*)$. The correlated portion of $\hat{g}_2(y_{\max_1}, y_{\max_2})$ becomes

$$\begin{aligned} \hat{p}(y_{\max_1}) \delta(y_{\max_1} - y_{\max_2}) = & \mathcal{N}_p \frac{1}{2} \left\{ \tanh \left(\frac{y_{\max_1} - y_{\text{cut}}^*}{\xi_{\text{cut}}} \right) + 1 \right\} \\ & \times e^{-(n_{\text{QCD}}^* - 2)(y_{\max_1} - y_{\text{cut}}^*)} (y_{\max_1} - y_{\min})^4 \\ & \times \delta(y_{\max_1} - y_{\max_2}) \end{aligned} \quad (80)$$

with normalization constant \mathcal{N}_p . Correlations are generated in this model when $0 < \gamma \leq 1$ and may be modified by allowing $n_{\text{QCD}}^* \neq n_{\text{QCD}}$ and/or $y_{\text{cut}}^* \neq y_{\text{cut}}$ where n_{QCD} and y_{cut} are determined by fitting the single particle p_t spectra as described in Sec. III A.

It is essential that the single-particle projection (marginal) of $\bar{\rho}_{hh}$ equal the single-particle, semi-hard component $\bar{\rho}_h(y_t)$ in order to maintain equality between the single-particle projection of the full, two-particle distribution in Eq. (64) and the measured charge distribution. This can be accomplished by requiring that

$$\int dy_{\max_2} \hat{g}_2(y_{\max_1}, y_{\max_2}) = \hat{g}(y_{\max_1}), \quad (81)$$

which in turn requires that function $\hat{h}(y_{\max})$ in Eq. (78) be determined by

$$\hat{h}(y_{\max}) = [\hat{g}(y_{\max}) - \gamma \hat{p}(y_{\max})] / (1 - \gamma), \gamma < 1 \quad (82)$$

as parameters n_{QCD}^* and y_{cut}^* in $\hat{p}(y_{\max})$ vary. Substituting the above quantities into Eq. (74) results in the “jet-jet” contribution to the same-event pair-distribution given in the continuum limit by

$$\begin{aligned} \bar{\rho}_{hh} &= \frac{\bar{N} - 1}{\bar{N}} (\bar{N}_h^2 + \sigma_0^2) \left[(1 - \gamma) \int dy_{\max_1} \hat{h}(y_{\max_1}) \hat{\rho}_{h, y_{\max_1}}(y_{t1}) \int dy_{\max_2} \hat{h}(y_{\max_2}) \hat{\rho}_{h, y_{\max_2}}(y_{t2}) \right. \\ &\quad \left. + \gamma \int dy_{\max} \hat{p}(y_{\max}) \hat{\rho}_{h, y_{\max}}(y_{t1}) \hat{\rho}_{h, y_{\max}}(y_{t2}) \right] \\ &\equiv \frac{\bar{N} - 1}{\bar{N}} (\bar{N}_h^2 + \sigma_0^2) \left[(1 - \gamma) \hat{\rho}_{\text{Jet[h]}}(y_{t1}) \hat{\rho}_{\text{Jet[h]}}(y_{t2}) + \gamma \hat{\rho}_{2\text{D-Jet[p]}}(y_{t1}, y_{t2}) \right], \end{aligned} \quad (83)$$

where $\hat{\rho}_{\text{Jet[h]}}$ and $\hat{\rho}_{2\text{D-Jet[p]}}$ in the last line are defined by the integrals in the first two lines of the equation. As usual, the above quantities are calculated at the y_t bin mid-points.

The “string-jet” cross terms do not contribute to the correlations when β and y_{\max} fluctuations are independent. These terms are readily given by

$$\bar{\rho}_{sh} = \frac{\bar{N} - 1}{\bar{N}} (\bar{N}_s \bar{N}_h - \sigma_0^2) \hat{\rho}_s(y_{t1}) \hat{\rho}_{\text{Jet[g]}}(y_{t2}) \quad (84)$$

where the event-averaged number of “string-jet” pairs equals $(\bar{N}_s \bar{N}_h - \sigma_0^2)$ if the event multiplicity is fixed and $\hat{\rho}_s(y_t)$ and $\hat{\rho}_{\text{Jet[g]}}(y_t)$ are unit-normalized versions of the corresponding average single-particle distributions in Eq. (63). Cross term $\bar{\rho}_{hs}$ is calculated by interchanging labels 1 and 2 in Eq. (84).

The remaining terms include products of the residual $\delta \bar{\rho}(y_t)$ with either $\hat{\rho}_s$, $\hat{\rho}_{\text{Jet[g]}}$ or itself, and are collected

into one term given by

$$\begin{aligned} \bar{\rho}_\delta \equiv & \frac{\bar{N}-1}{\bar{N}} \left\{ \delta\bar{\rho}(y_{t1}) [\bar{N}_s \hat{\rho}_s(y_{t2}) + \bar{N}_h \hat{\rho}_{\text{Jet}[g]}(y_{t2})] \right. \\ & + \delta\bar{\rho}(y_{t2}) [\bar{N}_s \hat{\rho}_s(y_{t1}) + \bar{N}_h \hat{\rho}_{\text{Jet}[g]}(y_{t1})] \\ & \left. + \delta\bar{\rho}(y_{t1}) \delta\bar{\rho}(y_{t2}) \right\}. \end{aligned} \quad (85)$$

Combining terms $\bar{\rho}_{ss}$, $\bar{\rho}_{hh}$, $\bar{\rho}_{sh}$, $\bar{\rho}_{hs}$ and $\bar{\rho}_\delta$ gives $\bar{\rho}_{\text{TCF,se}}$ in Eq. (64). The single-particle projection (marginal) of this two-particle distribution is given by

$$\begin{aligned} \bar{\rho}_{\text{TCF,marg}}(y_{t1}) &= \frac{1}{\bar{N}-1} \sum_{y_{t2}} \bar{\rho}_{\text{TCF,se}}(y_{t1}, y_{t2}) \\ &= \bar{N}_s \sum_{y_{t2}} \hat{\rho}_{\text{2D-Levy}}(y_{t1}, y_{t2}) \\ &\quad + \bar{N}_h \hat{\rho}_{\text{Jet}[g]}(y_{t1}) + \delta\bar{\rho}(y_{t1}). \end{aligned} \quad (86)$$

The per-pair normalized correlation quantity is given by

$$\begin{aligned} \frac{\Delta\bar{\rho}_{\text{TCF}}}{\bar{\rho}_{\text{ref}}}(y_{t1}, y_{t2}) &= \\ \frac{\bar{\rho}_{\text{TCF,se}}(y_{t1}, y_{t2}) - \frac{\bar{N}-1}{\bar{N}} \bar{\rho}_{\text{TCF,marg}}(y_{t1}) \bar{\rho}_{\text{TCF,marg}}(y_{t2})}{\bar{\rho}_{\text{ref}}(y_{t1}, y_{t2})}, \end{aligned} \quad (87)$$

analogous to Eq. (38), where $\bar{\rho}_{\text{ref}}$ is defined as the product of marginals [see Eq. (37)]. It is given by

$$\bar{\rho}_{\text{ref}}(y_{t1}, y_{t2}) = \frac{\bar{N}-1}{\bar{N}} \bar{\rho}_{\text{TCF,marg}}(y_{t1}) \bar{\rho}_{\text{TCF,marg}}(y_{t2}). \quad (88)$$

Using the soft-process prefactor in Eq. (40) for the charge-independent, away-side correlations gives the final correlation for the two-component fragmentation model:

$$\frac{\Delta\bar{\rho}_{\text{TCF}}}{\sqrt{\bar{\rho}_{\text{soft}}}}(y_{t1}, y_{t2}) = \mathcal{P}_{\text{Fac,soft}}^{\text{AS-CI}}(y_{t1}, y_{t2}) \frac{\Delta\bar{\rho}_{\text{TCF}}}{\bar{\rho}_{\text{ref}}}(y_{t1}, y_{t2}). \quad (89)$$

Finally, it is instructive to expand $\Delta\bar{\rho}_{\text{TCF}}(y_{t1}, y_{t2})$ in terms of the separate sources of correlations assumed in the model. Inserting Eqs. (73) and (83)-(86) into $\Delta\bar{\rho}_{\text{TCF}}$ in Eqs. (87) gives

$$\begin{aligned} \Delta\bar{\rho}_{\text{TCF}}(y_{t1}, y_{t2}) &= \frac{\bar{N}-1}{\bar{N}} [(\bar{N}_s^2 + \sigma_0^2) (\hat{\rho}_{\text{2D-Levy}}(y_{t1}, y_{t2}) - \hat{\rho}_s(y_{t1}) \hat{\rho}_s(y_{t2})) \\ &\quad + (\bar{N}_h^2 + \sigma_0^2) ((1-\gamma) \hat{\rho}_{\text{Jet}[h]}(y_{t1}) \hat{\rho}_{\text{Jet}[h]}(y_{t2}) + \gamma \hat{\rho}_{\text{2D-Jet}[p]}(y_{t1}, y_{t2}) - \hat{\rho}_{\text{Jet}[g]}(y_{t1}) \hat{\rho}_{\text{Jet}[g]}(y_{t2})) \\ &\quad + \sigma_0^2 (\hat{\rho}_s(y_{t1}) - \hat{\rho}_{\text{Jet}[g]}(y_{t1})) (\hat{\rho}_s(y_{t2}) - \hat{\rho}_{\text{Jet}[g]}(y_{t2}))]. \end{aligned} \quad (90)$$

Soft string-fragmentation induced correlations are represented in the first term and are controlled in the model via parameter $\Delta(1/q)_2 \equiv (1/2)[\Delta(1/q)_\Sigma - \Delta(1/q)_\Delta] = (1/q_{\beta_\Sigma} - 1/q_{\beta_\Delta})/2$ and the correlations scale with $(\bar{N}_s^2 + \sigma_0^2)$. The semi-hard scattering, correlated fragmentation contributions are represented in the second term and are controlled by parameter $\gamma \in [0, 1]$ and modulated by the two-particle, correlated semi-hard scattering probability distribution parameters y_{cut}^* and n_{QCD}^* in function $\hat{p}(y_{\text{max}})$ [see Eq. (80)]. The semi-hard scattering correlations scale with $(\bar{N}_h^2 + \sigma_0^2)$. The semi-hard scattering versus soft string-fragmentation multiplicity fluctuation variance, σ_0^2 , independently generates correlations when the soft and semi-hard process particle distribution shapes differ as given by the third term in Eq. (90).

IV. PHENOMENOLOGICAL MODEL CORRELATION RESULTS

The BW and TCF models were fitted to analytical representations of preliminary (y_{t1}, y_{t2}) charged-particle correlation data from STAR [20, 21]. The results are shown and discussed with respect to the efficacy of each model and the stability and systematic dependencies of the model parameters on centrality. The functional description of the pseudodata is discussed first, followed by discussions of the fitting results for the BW and TCF models.

A. Correlation pseudodata

Preliminary, total pair-number normalized, charged-particle correlations on (y_{t1}, y_{t2}) in the range $y_t \in [1.0, 4.5]$ for minimum-bias Au+Au collisions at $\sqrt{s_{NN}} = 200$ GeV from the STAR Collaboration were reported by Oldag [20, 21]. The data were fitted with a 2D-Levy

distribution [Eq. (73)] plus a constant offset and a 2D Gaussian. The correlations described with this model include all away-side, charged-pair combinations. The AS angular selection eliminates the enhanced correlation structure along the $y_{t1} = y_{t2}$ main-diagonal caused by quantum correlations between identical bosons [7] as discussed in [14]. The analytical fitting function is given by

$$\frac{\Delta\rho}{\sqrt{\rho_{\text{soft}}}}|_{\text{AS-CI}} = \mathcal{P}_{\text{Fac,soft}}^{\text{AS-CI}} \left(\frac{\hat{\rho}_{2\text{D-Levy}}^{\text{data}} - \hat{\rho}_{2\text{D-mix}}}{\hat{\rho}_{2\text{D-mix}}} \right) + A_0 + A_1 e^{-y_{t\Delta}^2/2\sigma_{\Delta}^2} e^{-(y_{t\Sigma}-2y_{t0})^2/2\sigma_{\Sigma}^2} \quad (91)$$

where the 2D-Levy distribution is the same as in Sec.III, Eq. (73) with parameters β_0 , q_{Σ} and q_{Δ} replacing parameters $\bar{\beta}$, $q_{\beta\Sigma}$ and $q_{\beta\Delta}$ in Eq. (73). The corresponding variance difference quantities are given by $\Delta(1/q)_{\Sigma,\Delta} = 1/q_{\Sigma,\Delta} - 1/q_{\text{fluct}}$. Also in Eq. (91) we introduced sum and difference variables $y_{t\Sigma,\Delta} = y_{t1} \pm y_{t2}$. The marginal of $\hat{\rho}_{2\text{D-Levy}}^{\text{data}}$ is given by

$$\hat{\rho}_{\text{marg}}(y_{t1}) = \sum_{y_{t2}} \hat{\rho}_{2\text{D-Levy}}^{\text{data}}(y_{t1}, y_{t2}) \quad (92)$$

and the mixed-event reference $\hat{\rho}_{2\text{D-mix}}(y_{t1}, y_{t2})$ is the product of marginals for particles 1 and 2.

The 2D-Levy distribution alone did not produce satisfactory descriptions of the data and was supplemented with a constant offset (A_0) plus a 2D Gaussian. Fit parameters $\Delta(1/q)_{\Sigma,\Delta}$, q_{fluct} , A_0 , A_1 , y_{t0} , σ_{Δ} and σ_{Σ} were interpolated from the trends plotted in Ref. [21], Fig. 5.14, at the mid-points of the centrality bins studied here. The 2D Gaussian widths along the difference direction $y_{t\Delta}$ exceeded the corresponding widths along $y_{t\Sigma}$. Physically, for the AS correlations this could be caused by initial-state transverse momentum, K_T , in the parton-parton collision frame, which imparts more p_t to the fragments of one jet than the other, resulting in a broadening along $y_{t\Delta}$ when summed over many dijets. Such additional, initial-state dynamics could be included in both the BW and TCF models but, for simplicity, was not accounted for in this initial “proof-of-principle” model study. The width σ_{Δ} in the pseudodata was therefore set equal to σ_{Σ} .

The correlation pseudodata were assigned statistical errors corresponding to the number of pairs per bin expected for the 9.5 million, 200 GeV minimum-bias Au+Au collisions in the data volume reported in [21]), for the observed charged-particle p_t, η distributions in centrality bins 0-5%, 5-10%, 10-20%, 20-30%, 30-40%, 40-60% and 60-80%, for single-particle acceptance $|\eta| \leq 1$, $p_t \geq 0.15$ GeV/c, full 2π azimuth, and assuming symmetric correlations with respect to $\pm|y_{t1} - y_{t2}|$. The latter symmetrization is valid when particles 1 and 2 are taken from the same collection of particles, for example all charged particles. This step is implemented by counting each unique particle pair in both bins with coordinates (y_{t1}, y_{t2}) and (y_{t2}, y_{t1}) . For diagonal bins (y_t, y_t) ,

only the $y_{t1} \geq y_{t2}$ half is used for calculating the statistical errors. Typical statistical errors (for $y_t \leq 3$) in more-central collisions vary from approximately 1% to 3% relative to the correlation amplitude at the peak near $(y_{t1}, y_{t2}) = (3, 3)$, increasing to 3% to 5% in more-peripheral collisions. The pseudodata were generated in each (y_{t1}, y_{t2}) bin by sampling a Gaussian distribution whose mean equals the calculated value in Eq. (91) and whose width parameter (σ) was equal to the estimated statistical error. The correlation pseudodata were binned on a uniform 25×25 2D grid for $y_t \in [1.0, 4.5]$ corresponding to $p_t \in [0.16, 6.3]$ GeV/c. Pseudodata were generated for (y_{t1}, y_{t2}) bins with $y_{t1} \geq y_{t2}$, and then copied to the (y_{t2}, y_{t1}) bin.

B. Blast-wave model description of correlations

The AS-CI correlation pseudodata were fit with the fluctuating blast-wave model in Eq. (39) using fit parameters $\Delta(1/q)_1$ and $\Delta(1/q)_2$ in Eq. (29) plus the transverse flow correlation parameter $\Delta\eta_t$ introduced in Eq. (32). Other parameters of the model including $\bar{\beta} = 1/T$, q_{β} , a_0 , n_{flow} and σ_{η_t} were determined by fitting the single-particle p_t spectrum data (see Table I) and were kept fixed. Fit parameters and statistical fitting errors are listed in Table IV. Pseudodata, BW model fits, and residuals (pseudodata - model) are shown for three example centrality bins (60-80%, 20-30% and 0-5%) in Fig. 3. The results show a smooth, monotonic centrality dependence from most-peripheral to most-central. The general features of the correlation structures, *e.g.* saddle-shape and peak near $(y_{t1}, y_{t2}) = (3, 3)$, are qualitatively reproduced by the model, however the (3,3) peak amplitude is underestimated by about 20-30%. Residuals are overall somewhat smaller than the data, differing mainly at lower y_t and near the (3,3) peak.

The best determined fit parameter is the inverse temperature co-variation $\Delta(1/q)_2$ which is always positive, corresponding to positive correlations in the temperature fluctuations, and which displays a monotonic decrease with centrality. Of the three fit parameters, $\Delta(1/q)_2$ has the smallest relative errors and displays the smoothest centrality trend. It should be pointed out that in conventional thermal models of relativistic heavy-ion collisions, larger systems are expected to more closely approach global, thermal equilibrium which would increase temperature correlations between intra-event emission points, resulting in larger $\Delta(1/q)_2$, not the decreasing trend shown in Table IV. The overall (β_1, β_2) distribution expansion/contraction parameter $\Delta(1/q)_1$ tends to decrease (*i.e.* a contraction) with more-central collisions but has larger, relative errors and greater variability than $\Delta(1/q)_2$. The transverse flow rapidity correlation fit parameters $\Delta\eta_t$ are non-negative, indicating flow correlations, but have relatively large uncertainties and erratic centrality dependence indicating that correlated transverse flow fluctuations are poorly determined.

An essential requirement of the BW correlation model is that the single-particle p_t distribution be preserved, regardless of how the fit parameters vary, in order to describe the correlation pseudodata. In the BW model, non-zero values of $\Delta(1/q)_1$ cause the single-particle marginal of the two-particle distribution to differ from the single-particle BW model fit to the p_t spectrum data. Small, non-zero values of $\Delta(1/q)_1$ are, however, helpful in fitting the correlations. To determine if the fitted, two-particle BW model distribution remains consistent with the single-particle p_t distribution, we constructed the single-particle projection of the two-particle BW model fit [Eq. (34)] and compared it to the charged-particle distribution and to the single-particle BW model fit. The two-particle projections were consistent with the single-particle BW fits for $y_t \leq 3$ for all centralities except the most-peripheral 60-80% case where significant differences occur for $y_t \geq 2.5$. The BW marginals differ from the p_t -spectrum data by $\leq 15\%$ throughout the entire y_t range studied here for all centralities except the most-peripheral with $y_t \geq 3$.

It is interesting to examine the degree of correlation in the inverse temperature and transverse flow rapidity sampled by arbitrary pairs of particles. Ratio $\sigma_\beta^2/\bar{\beta}^2$ is the relative variance of the inverse temperature distribution [Eq. (13)] for the single-particle distribution in Eq. (12). Defining $\delta_{\Sigma,\Delta}$ as the change in widths of the two-particle (β_1, β_2) distribution [Eq. (27)] along the $\beta_{\Sigma,\Delta} = \beta_1 \pm \beta_2$ directions, respectively, where $\delta_{\Sigma,\Delta} \equiv \sigma_{\beta_{\Sigma,\Delta}} - \sigma_\beta$, we may estimate the average, relative expansion or contraction of the (β_1, β_2) distribution as

$$\frac{\delta_\Sigma + \delta_\Delta}{2\bar{\beta}} \approx (\sqrt{q_\beta}/2)\Delta(1/q)_1, \quad (93)$$

for $\delta_{\Sigma,\Delta}/\bar{\beta} \ll 1$. Similarly, the average, relative co-variation in the (β_1, β_2) distribution is

$$\frac{\delta_\Sigma - \delta_\Delta}{2\bar{\beta}} \approx (\sqrt{q_\beta}/2)\Delta(1/q)_2. \quad (94)$$

The average, relative co-variation in the two-particle, transverse flow rapidity is equal to $\Delta_{\eta_t}/(2\sigma_{\eta_t})$ [Eq. (32)]. These three quantities are listed in Table IV. The fitting results show that, within this fluctuating BW model and for these AS-CI pseudodata, thermal fluctuation widths vary from about 2% expansion in peripheral collisions to less than 0.5% contraction in most-central collisions. Relative co-variations decrease monotonically from about 0.4% to 0.1% from peripheral to most-central. Transverse flow co-variations are non-negative but display variability with respect to collision centrality, showing no clear trend in these fitting results. These small, relative changes in widths of the inverse temperature and flow fluctuations imply that intra-event β, η_{t0} fluctuation magnitudes exceed the inter-event mean differences in the fluctuations as discussed in Ref. [14].

The BW model fits to the p_t spectrum data provide an estimate of the variance in the distribution of inverse p_t -slope parameters, or temperature in the BW approach.

It is informative to compare these empirical fluctuation magnitudes to that expected for equilibrated, relativistic hadron-gas models at kinematic decoupling, or “freeze-out,” when event-wise fluctuations in participant nucleon number are included. In relativistic hadron-gas models the energy density ε is proportional to the freeze-out temperature to the fourth power [47], $\varepsilon \propto T^4$. In hydrodynamic models the total energy among the interacting partons is proportional to the number of participant nucleons; at mid-rapidity the energy density is therefore proportional to $N_{\text{part}}^{1/3}$ [34]. Also, in hydrodynamic models the energy density at freeze-out includes both thermal and collective modes, but it is still reasonable to assume that $T^4 \propto N_{\text{part}}^{1/3}$. Event-wise fluctuations in N_{part} for events having the same centrality, for example as defined by the impact parameter or multiplicity, produce temperature fluctuations which, in turn, produce two-particle correlations on transverse momentum.

Numerical estimates can be carried out using the BW fit values for temperature from Table I and $N_{\text{part}}^{1/3}$ from Table II. A proportionality constant, $\alpha = \partial T^4/\partial N_{\text{part}}^{1/3} \approx 0.000015 \text{ GeV}^4$, results if the most-peripheral bin is excluded. The resulting relation

$$\frac{\partial N_{\text{part}}}{\partial T} = 12T^3 N_{\text{part}}^{2/3}/\alpha \approx \frac{\delta N_{\text{part}}}{\delta T}, \quad (95)$$

where δN_{part} and δT represent event-wise fluctuations, can be used to estimate the variance in the fluctuating freeze-out temperature caused by event-wise fluctuations in N_{part} . The latter fluctuations could be caused by statistical fluctuations among collisions having the same impact parameter. In terms of inverse temperature $\beta = 1/T$, the relative variance of fluctuations in β for a collection of similar events is given by

$$\langle (\delta\beta/\bar{\beta})^2 \rangle = \frac{\sigma_\beta^2}{\bar{\beta}^2} = \frac{1}{q_\beta} = \left[(12/\alpha)^2 T^8 N_{\text{part}}^{1/3} \right]^{-1}, \quad (96)$$

where brackets “ $\langle \rangle$ ” denote an average over events, $\bar{\beta} = \langle \beta \rangle$, and the Poisson limit, $\langle (\delta N_{\text{part}})^2 \rangle = N_{\text{part}}$, was assumed. Using the BW fitted temperatures in Eq. (96) and the above value of α , results in relative variances which are too small by more than 3-orders of magnitude compared to $1/q_\beta$ in Table I. The co-variations in relative variance, $\Delta(1/q)_2$ from the 2D BW model fits, are two-orders of magnitude larger than the above limit in Eq. (96). These large discrepancies suggest that additional, and much stronger dynamical fluctuations, whose effects must persist until freeze-out, are required in hydrodynamic scenarios in order to generate the larger p_t -slope fluctuations implied by the present BW model fits to the p_t spectra data and estimated (y_{t1}, y_{t2}) correlations. These results impose significant constraints on the initial-state, on the effective partonic interactions in transport models, and on the parameters controlling the hydrodynamic expansion.

TABLE IV: Blast-wave correlation model fit parameters to the 200 GeV Au+Au (y_{t1}, y_{t2}) AS-CI correlation pseudodata. Statistical fitting errors are in parentheses. Relative expansion/contraction and relative co-variations in the thermal and transverse expansion parameters are also listed as explained in the text.

Cent.(%)	$\Delta(1/q)_1$	$\Delta(1/q)_2$	Δ_{η_t}	$\frac{\chi^2}{\text{Dof}}$	$\frac{\delta_{\Sigma} + \delta_{\Delta}}{2\beta}$	$\frac{\delta_{\Sigma} - \delta_{\Delta}}{2\beta}$	$\frac{\Delta_{\eta_t}}{2\sigma_{\eta_t}}$
0-5	-0.00162(38)	0.000500(4)	0.000400(135)	12.39	-0.00364	0.00112	0.0039
5-10	-0.00055(20)	0.000600(23)	0.0 \pm 0.0009	14.46	-0.00122	0.00133	0
10-20	-0.00106(25)	0.000650(8)	0.00175(54)	26.64	-0.00229	0.00141	0.0265
20-30	-0.00160(43)	0.000850(21)	0.0 \pm 0.0026	26.29	-0.00335	0.00178	0
30-40	-0.00100(39)	0.00110(4)	0.0 \pm 0.0022	19.63	-0.00204	0.00225	0
40-60	+0.0020(6)	0.00140(5)	0.0 \pm 0.0008	18.09	+0.00391	0.00274	0
60-80	+0.0100(4)	0.00210(5)	0.0030(61)	11.19	+0.018	0.00377	0.075

C. Two-component fragmentation model description of correlations

The AS-CI correlation pseudodata were fit with the TCF model described in Sec. III with parameters $\Delta(1/q)_{1,2} = (1/2)[\Delta(1/q)_{\Sigma} \pm \Delta(1/q)_{\Delta}]$ [see Eqs. (29) and (73)], semi-hard multiplicity fluctuation variance σ_0^2 in Eq. (72), semi-hard scattering correlation amplitude γ in Eq. (78), and $\hat{p}(y_{\text{max}})$ probability distribution parameters y_{cut}^* and n_{QCD}^* in Eq. (80). Other parameters of the TCF model were determined by fitting the single, charged-particle p_t spectra data as discussed in Sec. III, or were taken from Ref. [3].

Ambiguities occurred in the χ^2 -minimization procedure in which the color-string fragmentation parameter $\Delta(1/q)_2$ could be either positive or negative, corresponding to a normal saddle-shape correlation as in Ref. [14], or an inverted saddle-shape, respectively. An inherent assumption of the TCF model is that hadron fragments from the same color-string will be correlated in transverse momentum, *i.e.* fragmenting color-strings with greater or lesser energy than average will tend to produce particle pairs with greater or lesser p_t , respectively, resulting in a positive correlation along the $y_{t1} \approx y_{t2}$ diagonal. Restricting $\Delta(1/q)_2 > 0$ excluded the inverted saddle solution and it was found that acceptable descriptions of the correlations required relatively small absolute magnitudes for both $\Delta(1/q)_1$ and $\Delta(1/q)_2$, similar to, or smaller than the corresponding 2D BW parameters in Table IV. To constrain and stabilize the χ^2 -minimization we fixed the $\Delta(1/q)_{1,2}$ parameters to the fitted values in Ref. [21] which were determined by fitting the function in Eq. (91) to the AS-CI data. With the soft-component fit parameters thus constrained the correlation pseudodata were readily described by varying the remaining semi-hard scattering parameters σ_0^2 , γ , y_{cut}^* and n_{QCD}^* .

The model fits and residuals are compared with the correlation pseudodata in Fig. 4 and the fit parameters are listed in Table V. Smooth, monotonic trends in the residuals and good, overall descriptions of the pseudodata were achieved. The fitted peak amplitudes at $(y_{t1}, y_{t2}) \approx (3, 3)$ are about 10% below the pseudodata. Color-string fragmentation parameters $\Delta(1/q)_1$ [21] are negative, indicating a slight, overall contraction in the widths of

the distribution of p_t -slope parameter β . This reduction is sufficiently small that the marginals of the two-particle distributions remain within 1% of the charged-particle distributions over the full y_t range [1.0, 4.5] for all centralities from 0-80%. Parameters $\Delta(1/q)_2$ from Ref. [21] monotonically decrease from peripheral to most-central collisions as was also found for the BW model fits. Semi-hard scattering parameters σ_0^2 and γ monotonically increase and decrease, respectively, from peripheral to most-central collisions, while parameters y_{cut}^* and n_{QCD}^* remain approximately constant. From the definition of the jet energy correlation function $\hat{p}(y_{\text{max}})$ in Eq. (80) we expect $(n_{\text{QCD}}^* - 2) \approx 2(n_{\text{QCD}} - 2)$. The fitted values of n_{QCD}^* vary from about 11 to 12 which are smaller than this estimated range that varies from 12 to 16 using the values for n_{QCD} in Table III. This indicates that the distributions of correlated, semi-hard scattering maximum fragment rapidities, represented by distribution $\hat{p}(y_{\text{max}})$, are weighted toward larger y_{max} values than the corresponding single particle, distributions $\hat{g}(y_{\text{max}})$. All in all, these results demonstrate that the TCF model is capable of providing qualitative descriptions of correlation data on transverse momentum with smooth, monotonic centrality dependence in the fitting parameters.

In Eq. (90) contributions to the correlated pair distribution $\Delta\hat{\rho}_{\text{TCF}}(y_{t1}, y_{t2})$ were separated into color-string fragmentation, semi-hard parton fragmentation, and semi-hard multiplicity fraction fluctuations. Neglecting the relatively small centrality dependence in the shape of the single-particle distribution $\hat{\rho}_{\text{Jet}[g]}(y_t)$, the centrality dependence in the last contribution in Eq. (90) is primarily proportional to variance σ_0^2 . The centrality dependence of σ_0^2 from Table V is approximately described by a power-law where

$$\sigma_0^2 \approx 0.17 N_{\text{bin}}^{1.19} \quad (97)$$

for the centrality range 0-60%. This distribution somewhat exceeds binary scaling. Similarly, the second contribution in Eq. (90) can be expanded in powers of γ , which

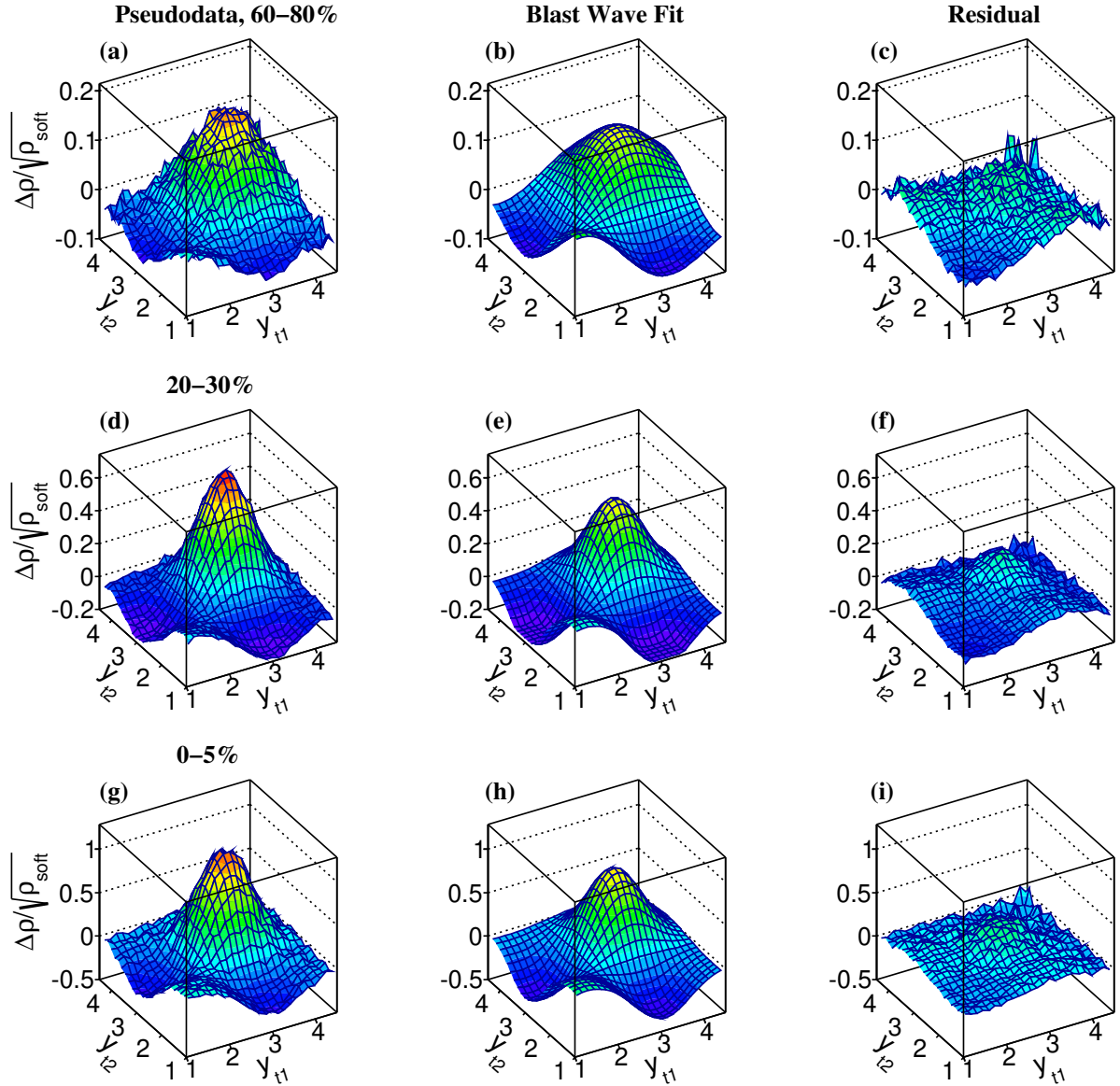


FIG. 3: Fluctuating blast-wave model fits to the 200 GeV Au+Au away-side, charge-independent two-particle correlation pseudodata described in Sec. IV A for selected centralities 60-80%, 20-30% and 0-5% in rows of panels from upper to lower, respectively. The left-hand column shows the pseudodata, the model results are shown in the middle column, and the residuals (pseudodata - model) are presented in the right-hand column.

to leading-order is given by the combination of terms

$$\begin{aligned}
 & \frac{\bar{N} - 1}{\bar{N}} (\bar{N}_h^2 + \sigma_0^2) \gamma \\
 & \times \left[\left(\hat{\rho}_{2D-Jet[p]}(y_{t1}, y_{t2}) - \hat{\rho}_{Jet[p]}(y_{t1}) \hat{\rho}_{Jet[p]}(y_{t2}) \right) \right. \\
 & \left. + \left(\hat{\rho}_{Jet[g]}(y_{t1}) - \hat{\rho}_{Jet[p]}(y_{t1}) \right) \left(\hat{\rho}_{Jet[g]}(y_{t2}) - \hat{\rho}_{Jet[p]}(y_{t2}) \right) \right], \quad (98)
 \end{aligned}$$

where $\hat{\rho}_{Jet[p]}$ is defined as in Eq. (58) using Eq. (78) and

is given by

$$\begin{aligned}
 \hat{\rho}_{Jet[p]}(y_t) & \equiv \int_0^\infty dy_{\max} \hat{\rho}(y_{\max}) \hat{\rho}_{h, y_{\max}}(y_t) \\
 & = \frac{1}{\gamma} \left[\hat{\rho}_{Jet[g]}(y_t) - (1 - \gamma) \hat{\rho}_{Jet[h]}(y_t) \right]. \quad (99)
 \end{aligned}$$

If the small centrality dependences of $\hat{\rho}_{Jet[g]}(y_t)$ and $\hat{\rho}_{Jet[p]}(y_t)$ are neglected, the number of correlated pairs in this contribution is approximately proportional to $(\bar{N}_h^2 + \sigma_0^2) \gamma \approx \bar{N}_h^2 \gamma$. From Table V we find that for the 0-40% more-central collisions, where γ becomes smaller,

the dependence of $(\bar{N}_h^2 + \sigma_0^2)\gamma$ can be approximated by

$$(\bar{N}_h^2 + \sigma_0^2)\gamma \approx 0.43N_{\text{bin}}^{1.44}. \quad (100)$$

Thus we find that empirical descriptions of the AS-CI correlation pseudodata, in terms of the TCF model, are consistent with a scenario in which the number of correlated particle pairs from semi-hard scattering and fragmentation processes increases smoothly with centrality and at a rate somewhat in excess of N+N binary scaling. Although these centrality trends in the parameters were determined by fits to pseudodata, it is expected that these results provide a reliable indication of how the TCF model will perform when applied to real data.

The contributions of the three terms in Eq. (90) for the 60-80%, 20-30% and 0-5% centrality bins are shown in Fig. 5 in comparison with the pseudodata. For the pure color-string fragmentation contribution, parameters σ_0^2 and γ were set to zero. For the pure semi-hard multiplicity fluctuation result, parameters $\Delta(1/q)_1$, $\Delta(1/q)_2$ and γ were set to zero. For the pure semi-hard fragmentation result, $\Delta(1/q)_1$, $\Delta(1/q)_2$ and σ_0^2 were set to zero. The results accurately represent the contributions of the first two terms in Eq. (90) to the extent that $\sigma_0^2 \ll \bar{N}_s^2$ and $\sigma_0^2 \ll \bar{N}_h^2$ which are true at the 1% amount or better (see Tables III and V), except for the 60-80% results. The color-string fragmentation contributes from about 20% of the predicted correlation peak amplitude at $(y_{t1}, y_{t2}) \approx (3, 3)$ in most-peripheral collisions to about 9% in most-central. The semi-hard scattering contributions [last two terms in Eq. (90)] together account for the remaining 80% to 91% of the predicted correlation peak in 60-80% and 0-5% centrality bins, respectively.

V. THEORETICAL MODEL PREDICTIONS

Predicted (y_{t1}, y_{t2}) correlations for two theoretical models which include event-wise fluctuations are shown in this section. The first, HIJING [27], provides a baseline prediction. In this model longitudinal fragmentation plus semi-hard parton scattering and jet fragmentation are assumed for heavy-ion collisions which are described as a sum of independent N+N interactions. The second, EPOS [25], includes soft and hard initial-stage interactions followed by hydrodynamic expansion and final-stage hadron + hadron scattering.

A. HIJING

The HIJING event-generator combines the longitudinally expanding color-flux tube LUND [1] model of hadronization plus PYTHIA [2] which generates semi-hard to hard perturbative QCD interactions with subsequent fragmentation into final-state particles. Each N+N interaction within a heavy-ion collision is treated independently and the particle production combined with

out further interactions. In its simplest application HIJING provides a null hypothesis for heavy-ion collisions as an independent superposition of nucleon + nucleon collisions.

For the present application two sets of 400K, 200 GeV minimum-bias Au+Au collision events were generated where jets were, and were not included, referred to as “jets on” and “jets off” in the following. LUND-model color-string fragmentation was included in both sets of simulations. The events were separated into 5 centrality bins based on charged-particle multiplicity within $|\eta| \leq 1$, full 2π azimuth and $p_t \geq 0.15$ GeV/c. The centrality bins 0-9%, 9-28%, 28-46%, 46-64% and 64-100% were selected to align with those used in the published 200 GeV Au+Au minimum-bias 2D angular correlations [31] corresponding to the (y_{t1}, y_{t2}) correlations in [20, 21]. The statistical quality of the simulated correlations limited the centrality dependence to these five bins.

The 2D (y_{t1}, y_{t2}) correlations were calculated as discussed in Sec. II C, Eqs. (38) - (42) where the same-event and reference pair distributions were calculated by the following event averages

$$\bar{\rho}_{\text{HIJ,se}}(y_{t1}, y_{t2}) = \frac{1}{\epsilon} \sum_{j=1}^{\epsilon} \frac{\bar{N}}{n_j} n_{\text{se},j}(y_{t1}, y_{t2}) \quad (101)$$

$$\bar{\rho}_{\text{HIJ,ref}}(y_{t1}, y_{t2}) = \frac{\bar{N} - 1}{\bar{N}\epsilon_{\text{mix}}} \sum_{j \neq j'} n_j(y_{t1}) n_{j'}(y_{t2}), \quad (102)$$

where the sums include all charged-particle pairs and all relative azimuth angles. In these definitions ϵ is the number of simulated events in the centrality bin, \bar{N} is the mean charged-particle multiplicity in acceptance $|\eta| \leq 1$, n_j is the event-wise multiplicity, $n_{\text{se},j}(y_{t1}, y_{t2})$ is the event-wise number of charged-particle pairs in event j in 2D bin at (y_{t1}, y_{t2}) , ϵ_{mix} is the number of simulated mixed-events, and $n_j(y_t)$ is the event-wise number of particles in arbitrary bin at y_t . The final, correlation quantity, suppressing y_t arguments for brevity, is given by

$$\frac{\Delta\bar{\rho}}{\sqrt{\bar{\rho}_{\text{soft}}}}|_{\text{HIJ}} = \sqrt{2}\mathcal{P}_{\text{Fac,soft}}^{\text{AS-CI}} \frac{\bar{\rho}_{\text{HIJ,se}} - \bar{\rho}_{\text{HIJ,ref}}}{\bar{\rho}_{\text{HIJ,ref}}} \quad (103)$$

where the soft-prefactor in Eq. (40) was computed using Levy model functions fitted to the p_t spectra from HIJING with either jets on or off. The leading $\sqrt{2}$ scales the AS-CI prefactor for the inclusion of both near-side and away-side pairs. The “soft” N_{part} -dependent component of the spectrum was estimated from the $N_{\text{part}} \rightarrow 2$ limit of the HIJING p_t spectra when jets were included. For the jets-off correlations the entire charged-particle distribution derives from “soft” processes, hence $d^2N_{\text{ch}}/dy_t d\eta = d^2N_{\text{ch,soft}}/dy_t d\eta$ and prefactor $\mathcal{P}_{\text{Fac,soft}}^{\text{AS-CI}}$ was computed accordingly.

Calculations of the pair averages in Eqs. (101) and (102) are susceptible to bias effects as explained in

TABLE V: Two-component fragmentation correlation model fit parameters to the 200 GeV Au+Au (y_{t1}, y_{t2}) AS-CI correlation pseudodata. Statistical fitting errors are in parentheses.

Cent.(%)	$\Delta(1/q)_1$	$\Delta(1/q)_2$	σ_0^2	γ	y_{cut}^*	n_{QCD}^*	$\frac{\chi^2}{\text{DoF}}$
0-5	-0.000285(47)	0.000415(60)	620(87)	0.042(2)	4.06(4)	11.4(1.3)	11.3
5-10	-0.000333(62)	0.000475(72)	540(64)	0.051(3)	4.08(5)	11.8(1.8)	13.5
10-20	-0.000382(62)	0.000535(70)	310(39)	0.061(2)	4.12(4)	11.5(1.4)	22.7
20-30	-0.000449(115)	0.000631(68)	190(17)	0.072(3)	4.16(6)	11.6(2.2)	22.7
30-40	-0.000635(144)	0.000876(92)	115(11)	0.102(4)	4.22(9)	11.8(3.8)	17.0
40-60	-0.001106(492)	0.001452(110)	31(7)	0.158(6)	4.06(11)	11.6(4.8)	13.8
60-80	-0.001964(1440)	0.002556(157)	51(9)	0.44(3)	4.18(18)	11.6(7.4)	9.4

Ref. [24]. These bias effects can be reduced by restricting the event-wise multiplicity range within which mixed-event pairs are constructed. In typical analyses, events within a broad centrality bin are sub-divided into several, narrower multiplicity bins; quantities $\bar{\rho}_{\text{HIJ,se}}$ and $\bar{\rho}_{\text{HIJ,ref}}$ are calculated using events only within a sub-bin; total pair-number weighted averages of the resulting ratios in each sub-bin give the final correlations. This procedure is especially important in more-central bins which tend to be much broader in multiplicity than peripheral and mid-central bins. However, the number of sub-bins had to be limited due to the statistical quality of the simulations, resulting in residual bias [24] in the 0-9% and 9-18% correlations. This bias appears as an offset [24] in the quantity $(\bar{\rho}_{\text{HIJ,se}} - \bar{\rho}_{\text{HIJ,ref}})/\bar{\rho}_{\text{HIJ,ref}}$ which for jets on (off) equaled 0.0014 and 0.005 (0.0016 and 0.004) for the 9-18% and 0-9% centralities, respectively. The bias was subtracted prior to multiplication by the prefactor in Eq. (103); it was not evident in the remaining centrality bins.

The predictions including all charged-particle pairs and all relative azimuth angles are shown in Fig. 6. The upper and middle rows of panels show the HIJING predictions with jets turned on and off, respectively. Centrality increases from left-to-right. The expected saddle shape is evident in both sets of predictions but especially in the jets-on predictions. Also, for jets on, the peaks near $(y_{t1}, y_{t2}) = (3, 3)$ increase monotonically with centrality while much smaller and more weakly increasing peak amplitudes are predicted when jets are turned off. With jets included the peak positions are located at $y_t \sim 3.0$ to 3.1, in agreement with the pseudodata. With jets off, the peak positions shift to lower y_t from about 2.5 to 3.0.

The HIJING predictions with jets on, although similar in structure to the pseudodata, have less than half the amplitude throughout most of the centrality range. The predicted peak amplitudes near $(y_{t1}, y_{t2}) = (3, 3)$ increase from approximately 0.13 in the 64-100% centrality bin, to about 0.4 in the 0-9% most-central bin, a factor of 3 increase. In comparison, the corresponding peaks in the pseudodata increase about a factor of 6 from most-peripheral to most-central.

In the most-peripheral bin the predicted correlations with jets on and the pseudodata are fairly similar in shape and overall amplitude. This could be an indication that the event-wise fluctuation mechanisms in HI-

JING are realistic in describing this type of correlation in peripheral collisions but soon fall out of favor as the real collisions become more complicated with increasing centrality. Clearly, the HIJING model without jet production is completely inadequate for describing p_t fluctuations in heavy-ion collisions at these energies [41].

B. EPOS

Hydrodynamic predictions for correlations on 2D transverse rapidity were studied using EPOS version 3.210(c) [25, 48]. In this model the initial collision stage is described via soft and hard-scattered Pomerons, including gluon saturation effects. Initial-stage color flux-tubes, or color-strings, which evolve from the Pomerons, are separated into “core” and “corona” domains based on their transverse momentum and the local string-density in the transverse plane [49]. Subsequent evolution of the initial-stage core region is described using (3+1)-D viscous hydrodynamics until hadronization. Final-stage hadronic scattering and reactions for both core and corona hadrons are described with UrQMD [50].

A total of 200K minimum-bias 200 GeV Au+Au collisions were generated [51] and separated into the same five centrality bins used for the HIJING results in the previous subsection. The same correlation quantity defined above in Eqs. (101) - (103) was used for the EPOS predictions. The EPOS single-particle p_t spectra were used to calculate the prefactor. Statistical limitations again restricted the multiplicity sub-binning, resulting in bias offsets of 0.001 and 0.0055 in the 9-28% and 0-9% centrality bins, respectively. As in the HIJING calculations, the bias offset was subtracted before multiplying by the prefactor.

Predictions are shown in the lowest row of panels in Fig. 6 where saddle shapes are evident as well as monotonically increasing peaks near $(y_{t1}, y_{t2}) = (3, 3)$ which increase a factor of approximately 6 from the 46-64% centrality bin to the most-central 0-9% bin. In the two, more-peripheral bins the EPOS predicted peaks are lower than the HIJING jets-on predictions and the pseudodata; the EPOS prediction for the most-peripheral bin is quite dissimilar from the pseudodata in overall shape. However, for the two more-central bins the EPOS predicted

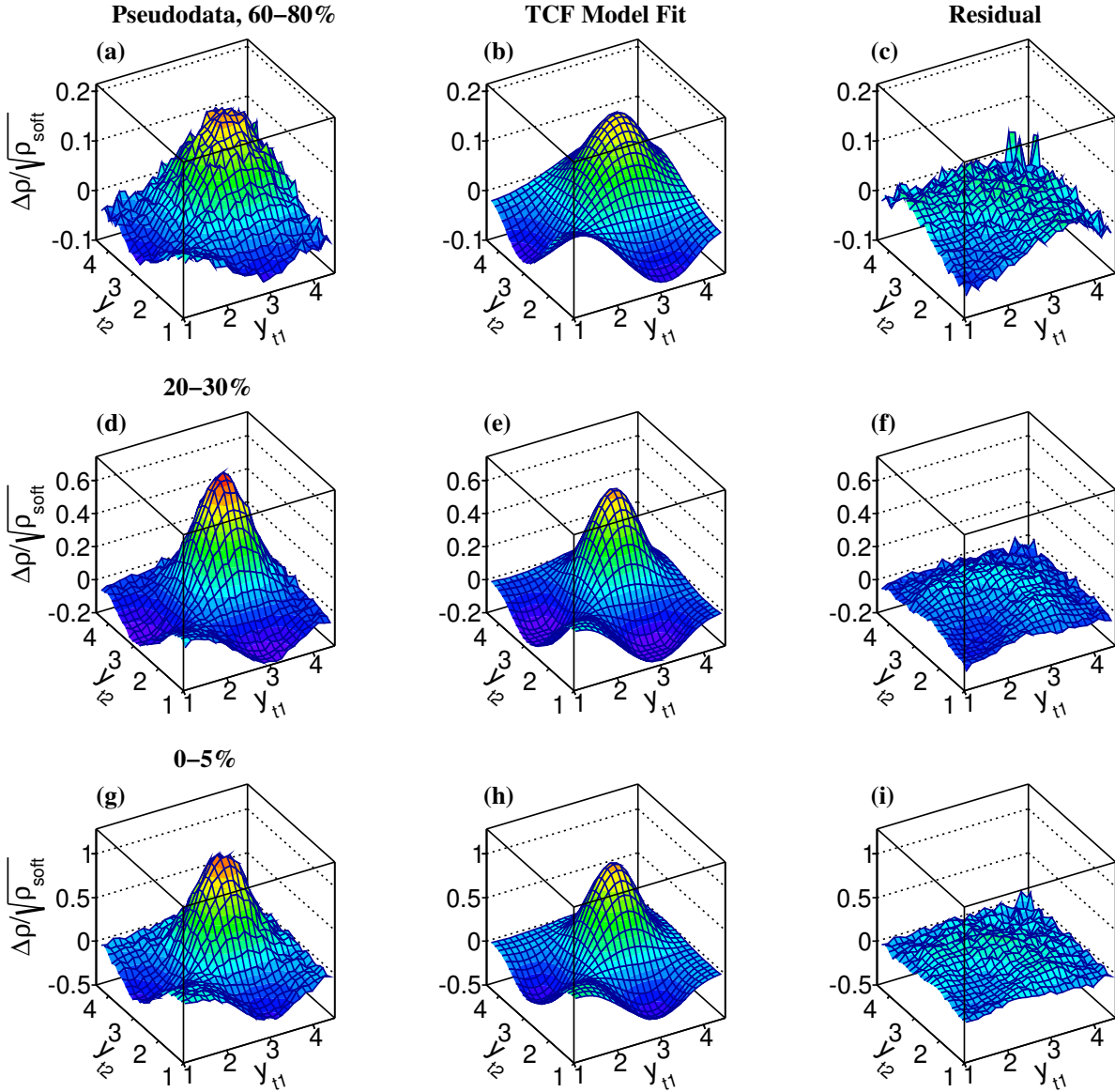


FIG. 4: Same as Fig. 3 except for the TCF model.

peak amplitudes are almost twice as large as the HIJING jets-on peaks. The EPOS predicted peaks also display a more realistic overall shape, and is closer in overall amplitude to the pseudodata. The off-diagonal minima at $(y_{t1}, y_{t2}) = (1, 3)$ for the EPOS predicted more-central bins are not nearly as deep as that in the pseudodata.

VI. SUMMARY AND CONCLUSIONS

The study of relativistic heavy-ion collisions has greatly benefited from the plethora of two-particle correlation measurements and analysis spanning the past few decades [8]. The vast majority of these correlation studies has focused on angular correlations where the p_t ranges

of the particles are often selected to be within kinematic regions of interest. Complementary correlation measurements on 2D transverse momentum are relatively scarce in the literature; analysis and interpretation of the few, observed correlation structures have been hampered by the absence of phenomenological models.

In this work we developed two phenomenological models based on fundamentally different assumptions about the dynamical evolution of the collision system. The first is based on a hydrodynamic expansion assumption as parametrized in the blast-wave model in which correlated, event-wise fluctuations in the temperature and transverse flow at kinematic freeze-out are included in order to generate two-particle correlations in the final-state. The second is based on the assumption that the

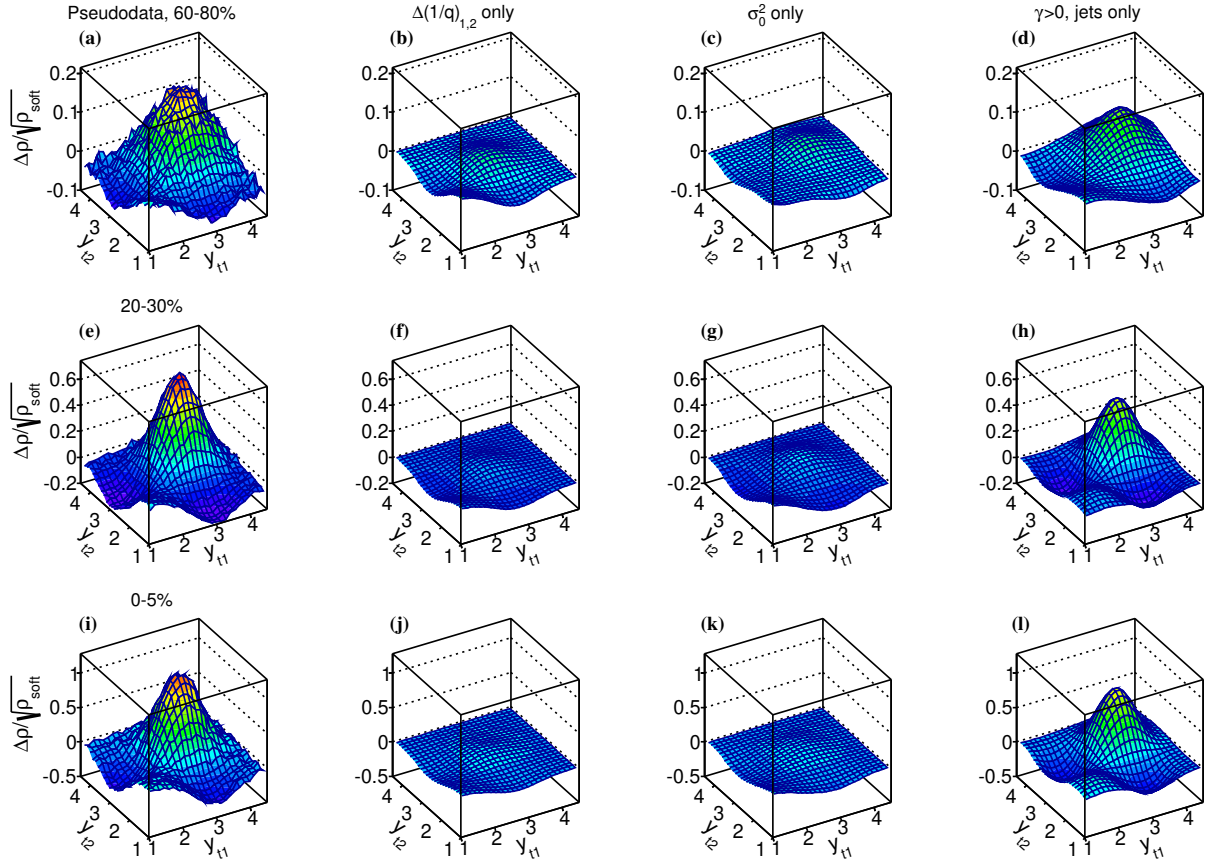


FIG. 5: Separated contributions to the fluctuating TCF model fits to the 200 GeV Au+Au away-side, charge-independent two-particle correlation pseudodata for selected centralities 60-80%, 20-30% and 0-5% in rows of panels from upper to lower, respectively. The left-hand column of panels shows the pseudodata. Fluctuation contributions from color-strings, semi-hard multiplicity production, and semi-hard fragmentation are shown in the second, third and fourth columns of panels, respectively, as explained in the text.

two-particle correlations are predominantly generated by soft- and semi-hard QCD scattering and fragmentation in which the energy and relative numbers of soft versus semi-hard processes fluctuate.

We demonstrated that both models provide quantitative descriptions of the measured charged-particle p_t spectra produced in $\sqrt{s_{NN}} = 200$ GeV Au+Au minimum-bias collisions. Using analytic representations of preliminary two-particle correlations on 2D transverse rapidity from the STAR Collaboration [20, 21], we demonstrated that both models qualitatively describe the correlations and for the most part result in smooth, monotonic centrality dependent trends in the fluctuation parameters used to fit the data.

The results of this “proof of principle” study already impose new constraints on both dynamical frameworks. In the hydrodynamic, BW approach we found that statistical fluctuations in the number of participant nucleons from event-to-event, as the sole source of final-state fluctuations in the p_t distribution, are much too small to account for the correlation structures. Much larger, dynamical fluctuations, whose effects persist until kinetic

freeze-out, are required. These results also imply that the magnitudes of intra-event fluctuations exceed the inter-event mean differences in fluctuations, which may impose limitations on the spatial scale of thermodynamic equilibration in such models. In the two-component fragmentation approach we found that the semi-hard scattering and fragmentation induced correlations required to describe the data appear to exceed binary scaling which suggests additional, multi-parton dynamics in the initial-state or during fragmentation within the dense medium.

Finally, we compared the predictions of an event-by-event (3+1)-dimensional hydrodynamic code EPOS and the soft plus hard-scattering and fragmentation code HIJING to each other and to the structures in the pseudodata. Both theoretical models produced correlation structures similar in overall shape to each other and to the pseudodata, where hard scattering is clearly required in HIJING. The HIJING predictions, with jets on, for the most-peripheral centrality bin are quite similar to the pseudodata in both overall shape and amplitude, while the EPOS prediction for the shape of the most-central correlation is similar to the pseudodata, but smaller in

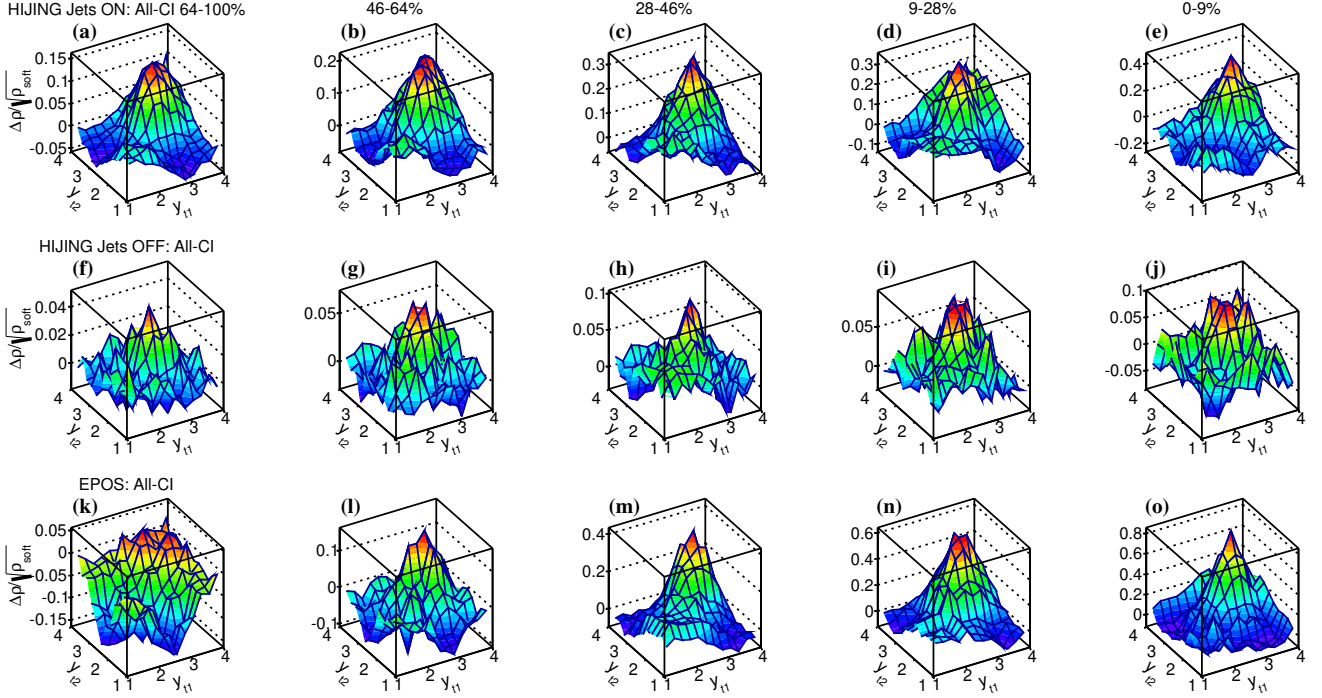


FIG. 6: HIJING model predictions for 200 GeV Au+Au collisions with jets on (upper row of panels) and jets off (middle row of panels) for all-azimuth, charge-independent two-particle correlations on transverse rapidity. Results for five centralities are shown in each row from left-to-right for cross section fractions 64-100%, 46-64%, 28-46%, 9-28% and 0-9%, respectively. EPOS predictions are similarly shown in the last row.

overall amplitude.

The BW and TCF phenomenological models developed here will be used in future analysis of two-particle correlation measurements on transverse rapidity from the STAR Collaboration. Ultimately, application of these phenomenologies may find that the fluctuation magnitudes required to describe the data cannot be justified within one or both of the dynamical frameworks considered here, thus falsifying the underlying approach. At the least, both phenomenological models can be used to constrain the magnitude and type of fluctuations required to describe the (y_{t1}, y_{t2}) correlations within their respective frameworks.

Acknowledgements

The authors would like to thank Professor Thomas Trainor of the Univ. of Washington for many informative discussions relevant to this work and Professor Rainer Fries of Texas A&M University for discussions related to the blast-wave model. We also thank Dr. Anders Knospe for providing the EPOS simulations. This research was supported in part by the Office of Science of the U. S. Department of Energy under Grants No. DE-FG02-94ER40845 and No. DE-SC0013391.

-
- [1] B. Andersson, G. Gustafson, G. Ingelman and T. Sjöstrand, Phys. Rep. **97**, 31 (1983).
 - [2] T. Sjöstrand and M. van Zijl, Phys. Rev. D **36**, 2019 (1987).
 - [3] T. A. Trainor, Phys. Rev. C **80**, 044901 (2009); T. A. Trainor and D. T. Kettler, Phys. Rev. D **74**, 034012 (2006).
 - [4] D. Teaney, J. Lauret and E. Shuryak, Phys. Rev. Lett. **86**, 4783 (2001); P. F. Kolb, U. Heinz, P. Huovinen, K. J. Eskola and K. Tuominen, Nucl. Phys. A **696**, 197 (2001); U. Heinz, J. Phys. G: Nucl. Part. Phys. **31**, S717 (2005); P. Huovinen and P. V. Ruuskanen, Annu. Rev. Nucl. Part. Sci. **56**, 163 (2006).
 - [5] E. Levin and A. Rezaeian, Phys. Rev. D **84**, 034031 (2011).
 - [6] R. L. Ray, Phys. Rev. D **90**, 054013 (2014).
 - [7] U. A. Wiedemann and U. Heinz, Phys. Rep. **319**, 145 (1999).
 - [8] T. A. Trainor, “A critical review of RHIC experimental results,” Int. J. Mod. Phys. E **23**, 1430011 (2014); arXiv:1303.4774.
 - [9] J. Adams *et al.* (STAR Collaboration), Phys. Rev. Lett. **95**, 152301 (2005).
 - [10] J. G. Reid, Nucl. Phys. A **698**, 611c (2002).

- [11] S. V. Afanasiev *et al.* (NA49 Collaboration), Nucl. Phys. A **715**, 55c (2003); T. Anticic *et al.* (NA49 Collaboration), Phys. Rev. C **70**, 034902 (2004).
- [12] D. Adamová *et al.* (CERES Collaboration), Nucl. Phys. A **811**, 179 (2008).
- [13] J. G. Reid, Ph.D. thesis, University of Washington, 2002 (unpublished); arXiv:nucl-ex/0302001.
- [14] J. Adams *et al.* (STAR Collaboration), J. Phys. G: Nucl. Part. Phys. **34**, 799 (2007).
- [15] T. A. Trainor and D. J. Prindle, Phys. Rev. D **93**, 014031 (2016).
- [16] J. Adams *et al.* (STAR Collaboration), Phys. Lett. B **634**, 347 (2006).
- [17] M. Aaboud *et al.* (ATLAS Collaboration), Phys. Rev. C **95**, 064914 (2017).
- [18] J. Adams *et al.* (STAR Collaboration), J. Phys. G: Nucl. Part. Phys. **32**, L37 (2006).
- [19] J. Adams *et al.* (STAR Collaboration), J. Phys. G: Nucl. Part. Phys. **34**, 451 (2007).
- [20] E. W. Oldag (STAR Collaboration), J. Phys.: Conf. Ser. **446**, 012023 (2013).
- [21] E. W. Oldag, Ph.D. thesis, The University of Texas at Austin, 2013 (unpublished), https://drupal.star.bnl.gov/STAR/files/oldag-dissertation_20132.pdf.
- [22] P. Bhattarai, Ph.D. thesis, The University of Texas at Austin, 2016 (unpublished), <https://drupal.star.bnl.gov/STAR/files/PhDThesisPrabhat-3.pdf>.
- [23] D. T. Kettler, D. J. Prindle and T. A. Trainor, Phys. Rev. C **91**, 064910 (2015).
- [24] R. L. Ray and P. Bhattarai, Phys. Rev. C **94**, 064902 (2016).
- [25] K. Werner, Nucl. Phys. B (Proc. Suppl.) **175-176**, 81 (2008).
- [26] T. Lappi and L. McLerran, Nucl. Phys. A **772**, 200 (2006); F. Gelis and R. Venugopalan, Acta Phys. Polon. B **37**, 3253 (2006).
- [27] X.-N. Wang, M. Gyulassy, Phys. Rev. D **44**, 3501 (1991).
- [28] E. Schnedermann, J. Sollfrank, U. Heinz, Phys. Rev. C **48**, 2462 (1993).
- [29] B. Tomášik, U. A. Wiedemann, U. W. Heinz, Acta Phys. Hung. A **17**, 105 (2003); arXiv:nucl-th/9907096 v1 (1999).
- [30] D. Kharzeev and M. Nardi, Phys. Lett. B **507**, 121 (2001); D. Kharzeev, E. Levin and M. Nardi, Nucl. Phys. A **730**, 448 (2004).
- [31] G. Agakishiev *et al.* (STAR Collaboration), Phys. Rev. C **86**, 064902 (2012).
- [32] L. Adamczyk *et al.* (STAR Collaboration), Phys. Lett. B **751**, 233 (2015).
- [33] Z. Yang and R. J. Fries, J. Phys. Conf. Ser. **832**, no.1, 012056 (2017); arXiv:1612.05629 [nucl-th].
- [34] J. D. Bjorken, Phys. Rev. D **27**, 140 (1983).
- [35] B. B. Back *et al.*, Phys. Rev. Lett. **91**, 052303 (2003).
- [36] M. Anderson *et al.*, Nucl. Instrum. Meth. Phys. Research A **499**, 659 (2003).
- [37] Y. Hama, T. Kodama and O. Socolowski, Jr., Braz. J. Phys. **35**, 24 (2005); W. L. Qian *et al.*, Braz. J. Phys. **37**, 767 (2007).
- [38] G. Wilk and Z. Włodarczyk, Phys. Rev. Lett. **84**, 2770 (2000).
- [39] J. Adams *et al.* (STAR Collaboration), Phys. Rev. Lett. **91**, 172302 (2003).
- [40] B. I. Abelev *et al.* (STAR Collaboration), Phys. Rev. C **79**, 034909 (2009).
- [41] J. Adams *et al.* (STAR Collaboration), Phys. Rev. C **71**, 064906 (2005).
- [42] J. L. Rodgers and W. A. Nicewander, Am. Stat. **42**, 59 (1988); B. S. Everitt and A. Skrondal, *The Cambridge Dictionary of Statistics*, 4th ed. (Cambridge University Press, Cambridge, 2010), p. 107.
- [43] T. A. Trainor, Int. J. Mod. Phys. E **17**, 1499 (2008); arXiv:0710.4504.
- [44] S. S. Adler *et al.* (PHENIX Collaboration), Phys. Rev. C **69**, 034910 (2004).
- [45] W. Braunschweig *et al.* (TASSO Collaboration), Z. Phys. C **47**, 187 (1990); M. Z. Akrawy *et al.* (OPAL Collaboration), Phys. Lett. B **247**, 617 (1990).
- [46] D. Acosta *et al.* (CDF Collaboration), Phys. Rev. D **68**, 012003 (2003).
- [47] B. Müller, "The Physics of the Quark-Gluon Plasma," *Lecture Notes in Physics*, No. 225, ed. by H. Araki, J. Ehlers, K. Hepp, R. Kippenhahn, H. A. Weidenmüller and J. Zittartz, (Springer-Verlag, Berlin, 1985).
- [48] K. Werner and G. Sophys, priv. comm.
- [49] K. Werner, B. Guiot, Iu. Karpenko, T. Pierog, Phys. Rev. C **89**, 064903 (2014).
- [50] H. Sorge, H. Stöcker, W. Greiner, Nucl. Phys. A **498**, 567 (1989); Ann. Phys. (N.Y.) **192**, 266 (1989).
- [51] A. Knospe, priv. comm.